SSI-DT79115040

Doctoral Thesis

A Study on Robust SEM Photometric Stereo Using Two BSE Detectors

Deshan Chen

March, 2014

Division of Systems Science and Informatics
Graduate School of Information Science and Technology
Hokkaido University

Doctoral Thesis
submitted to Graduate School of Information Science and Technology,
Hokkaido University
in partial fulfillment of the requirements for the degree of
Doctor of Philosophy.

Deshan Chen

Thesis Committee: Shun'ichi Kaneko Professor
Masahiko Onosato Professor
Takayuki Tanaka Associated Professor

A Study on Robust SEM Photometric Stereo Using Two BSE Detectors*

Deshan Chen

Abstract

This thesis presents a novel robust SEM photometric stereo method using two backscattered electron detectors. Robustness is one of the most important factors for practical applications. Although SEM photometric stereo has gained a lot of attention and been extensively studied, the robustness remains a very interesting challenge. Among ill factors, we realize that shadowing and noise problems are almost inherent in SEM photometric stereo. In particular, the shadowing effects generally give rise to significant errors in the reconstructed shapes. The present work is thereby devoted to developing SEM photometric stereo so that it can automatically handle such ill factors.

For dealing with shadowing effects, we introduce a shadowing compensation model though modeling image intensities in both cases of absence and presence of shadowing based mainly on angle distribution of backscattered electrons. This model relates the underlying shadowless image to the observed one by the corresponding detection ratio. The detection ratio has modeled the shadowing generation process by means of shadowing angles, which reflects the amount of occluded backscattered electrons. One advantage of the shadowing compensation model is that it is no need for us to treat the regions with shadowing errors separately from those without such errors, because the shadowless case is the special case of shadowing. Therefore, in contrast to some other approaches, the proposed method does not require an image segmentation process to extract shadowing regions, which is substantially difficult to implement automatically. The model has already provided an important cue to eliminate shadowing errors by means of inferring the shadowless images from the observed one if the shadowing angles can be obtained.

With the shadowing compensation model and gradient estimation equation, we formulate the proposed robust shape reconstruction into a constrained optimization problem via a variational approach. The objective functional consists of two terms. One is the fidelity term that is to guarantee the gradient of reconstructed shape should be consistent with the gradient data. In particular, the gradient data are evaluated from shadowless images so as to eliminate shadowing errors. In addition, shadowless images are related to the corresponding observed ones through our shadowing compensation

*Doctoral Thesis, Division of Systems Science and Informatics, Graduate School of Information Science and Technology, Hokkaido University, SSI-DT79115040, March 25, 2014.

model, which forms the constraints. The second term is total variation prior to penalize the roughness of the solution and consequently make our method be robust to noise influence arising in the data term. We adopt an iterative scheme to solve the problem, which performs commutatively between the compensation of image intensities and the modification of the corresponding 3D shape, can effectively provide both an accurate 3D shape and compensated shadowless images after convergence.

We present an extension to the shadowing compensation model in order to improve the model accuracy in the shadowing regions on the general curved surfaces. The extended model removes the earlier restrictive assumption that the shadowing effects exist only on horizontal surfaces. This model is developed in an analogous way through modeling image intensities in both the absence and presence of shadowing. A numerical solution is proposed to resolve the implicit expressions for double integrals in the model. Compared to the previous shadowing compensation model, the extended model can be more accurate when applied to shadowing regions on surfaces having large inclinations.

Experimental results demonstrate the robustness and effectiveness of our proposed methods. Compared to the traditional methods, reconstructed 3D shapes can achieve higher accuracy. Furthermore, the resulting compensated images provide a potential opportunity for improving the imaging performance of SEM devices.

Keywords: Scanning Electron Microscope (SEM), Shape Reconstruction, Shadowing Compensation model, Backscattering Electron, Variational Method

Contents

List of Figures

List of Tables

Chapter 1. Introduction

The scanning electron microscope (SEM) is a very important tool for observing microstructures ranging from millimeters to nanometers and has been widely used in the areas of medical observation, semiconductors, material analysis, etc. Compared with other common microscopies, SEM offers a unique combination of imaging characteristics including high lateral resolution, broad magnification range, and large depth of field. As the working mechanism of SEM, a focused electron beam, named primary beam (PE), scans across the surface of a specimen rectilinearly, and the generated electrons (secondary or backscattered electrons) from the beam-specimen interaction are detected synchronically from pixel to pixel with various intensities resulting in the image contrast.

Currently, the need for three-dimensional (3D) surface measurements is significantly increasing. In particular, quantitative measurements of specimen at micro- and nanoscales by a truly three dimensional characterization technique are highly demanded in a variety of applications such as high aspect ratio MEMS structures [33], surface roughness determination [34], nano-materials and nano-devices, life sciences, fracture analysis [35], and many others. As a representative instance, 3D shape information can provide valuable clues for inspecting and analyzing defects in products of semiconductor manufacturing processes, such as recognition of device patterns and defect regions, classification of defects in terms of the processes responsible for their generation (surface/embedded defects [1]) and the impact on electric properties (volume or shorting/disconnection defect), and specification and control of the issue process, etc.

1.1 Scanning process and image formation

Figure 1.1 shows a schematic diagram of SEM. In a typical SEM, an electron beam is thermionically emitted from an electron gun fitted with a tungsten filament cathode. Tungsten is normally used in thermionic electron guns because it has the highest melting point and lowest vapour pressure of all metals, thereby allowing it to be heated for electron emission, and because of its low cost. Other types of electron emitters include lanthanum hexaboride cathodes, which can be used in a standard tungsten filament SEM if the vacuum system is upgraded and FEG, which may be of the cold-cathode type using tungsten single crystal emitters or the thermally assisted Schottky type, using emitters of zirconium oxide.

The electron beam, which typically has an energy ranging from 0.2 keV to 40 keV, is focused by one or two condenser lenses to a spot about 0.4 nm to 5 nm in diameter. The

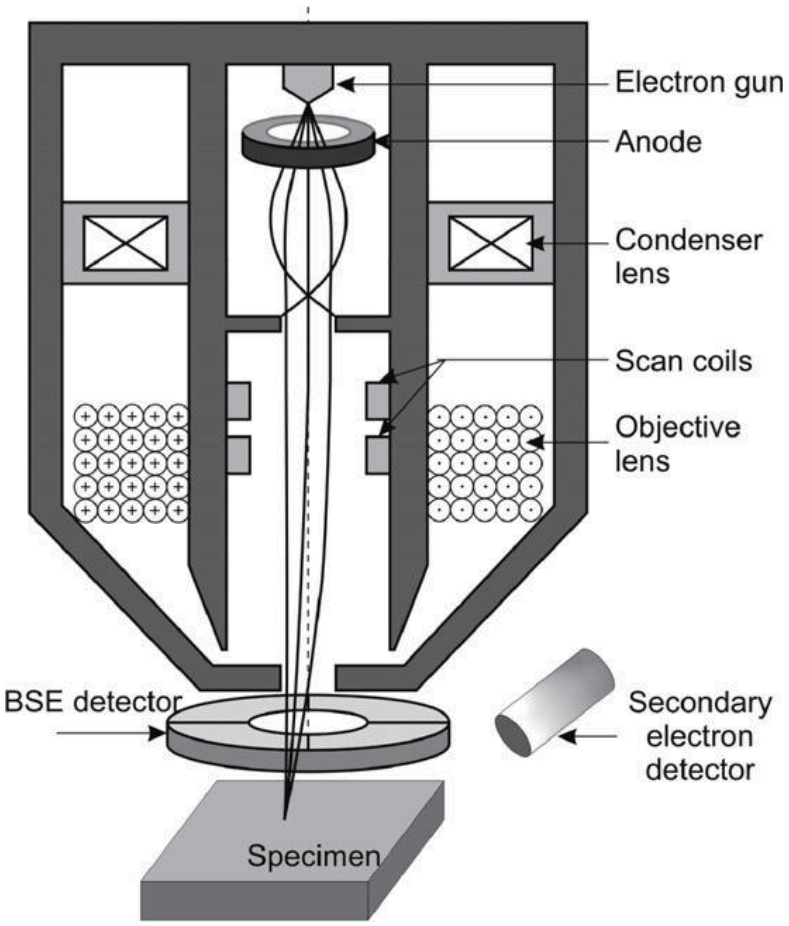

Figure 1.1: Schematic diagram of SEM.

beam passes through pairs of scanning coils or pairs of deflector plates in the electron column, typically in the final lens, which deflect the beam in the x and y axes so that it scans in a raster fashion over a rectangular area of the sample surface.

When the primary electron beam interacts with the sample, the electrons lose energy by repeated random scattering and absorption within a teardrop-shaped volume of the specimen known as the interaction volume, which extends from less than 100 nm to approximately 5 μm into the surface. The size of the interaction volume depends on the electron's landing energy, the atomic number of the specimen and the specimen's density. The energy exchange between the electron beam and the sample results in the reflection of high-energy electrons by elastic scattering, emission of secondary electrons by inelastic scattering and the emission of electromagnetic radiation, each of which can be detected by specialized detectors. The beam current absorbed by the specimen can also be detected and used to create images of the distribution of specimen current. Electronic amplifiers of various types are used to amplify the signals, which are displayed as variations in brightness on a computer monitor (or, for vintage models, on a cathode ray tube). Each pixel of computer videomemory is synchronized with the position of

the beam on the specimen in the microscope, and the resulting image is therefore a distribution map of the intensity of the signal being emitted from the scanned area of the specimen. In older microscopes image may be captured by photography from a high-resolution cathode ray tube, but in modern machines image is saved to a computer data storage.

1.2 Overview of 3D Reconstruction in SEM

In fact, SEM can only produce 2D images rather than 3D shape directly. Attempts have been made to transform SEM into a 3D measuring tool for over 30 years, and scientific research on 3D surface reconstruction in SEM continues to be intensively studied. Different approaches, which can be broadly classified into two groups, have been utilized. One group is generally referred to as the photogrammetry method, the other is the so-called SEM photometric stereo method.

1.2.1 Photogrammetry Approaches

Photogrammetry method [2, 3, 4, 26, 27, 28], in which a pair of stereo images of a specimen at different inclination angles are taken, and the shape or depth is determined by measuring the deviations of corresponding points on the two images. However, this method can only be applied to the measurements of surface points where recognizable fine structures exist. In general, it cannot be used on smooth surfaces or to reconstruct a continuous surface profile at high magnification.

1.2.2 Photometric Stereo Approaches

An alternative approach, that can applicable to smooth shape as well, is the so-called SEM photometric stereo method, in which multiple secondary or backscattered electron detectors (generally two or four) are symmetrically positioned about the beam axis, so that the gradient information on the surface being observed can be estimated from multiple images that are measured simultaneously by multiple detectors [5, 6, 7, 8, 9, 10]. The 3D surface is consequently obtained from the gradient information.

1.2.3 General Problems

Most of previous studies on SEM photometric stereo have focused almost exclusively on deriving accurate gradient measurement formulas, i.e., expressions of the relationships between the gradient component of target objects and the measured SEM signals from multiple detectors at the points of observation. Despite of extensive studies, robustness remains a very interesting challenge to make the technique be more practically applicable. As SEM photometric stereo making use of shading cues to infer 3D shapes, it is clear that

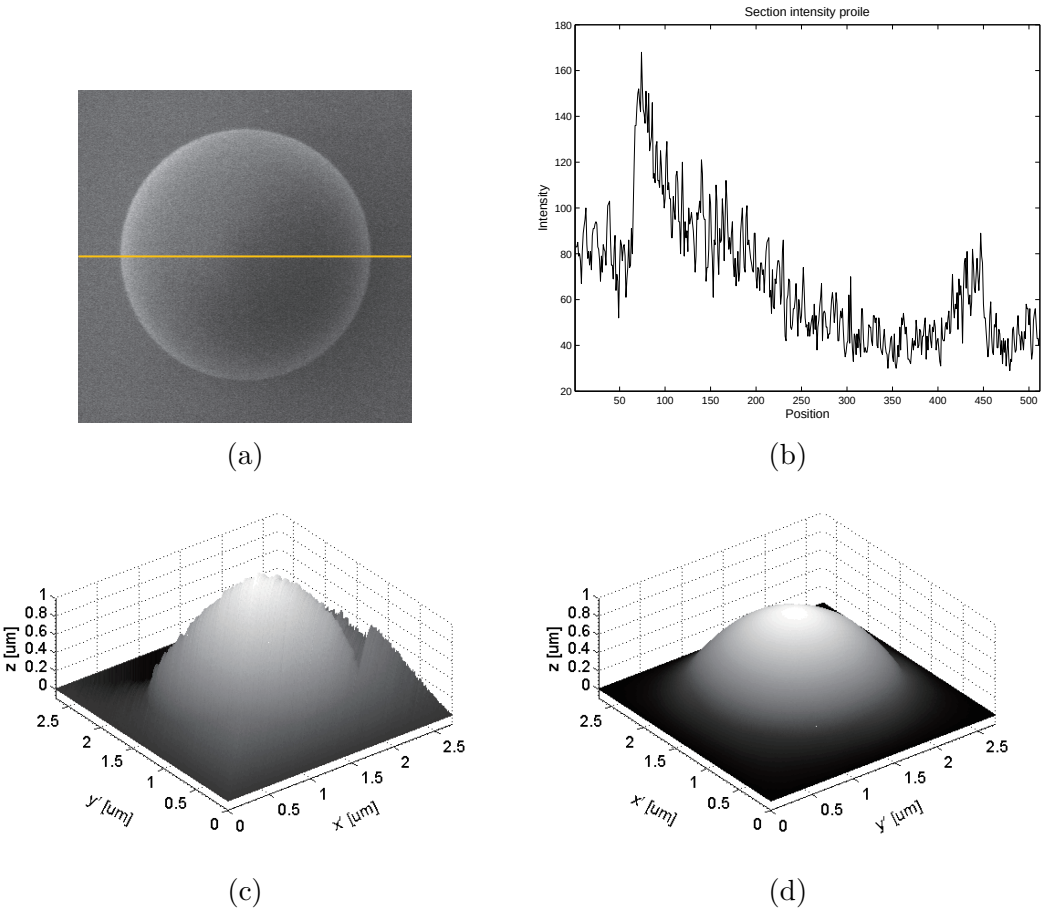

Figure 1.2: Noise effect. (a) Original left image of a sphere pattern, (b) intensity profile of the center section marked on (a), (c) 3D shape reconstructed via numerical integration and (d) 3D shape reconstructed via our proposed variational method.

the accuracy of images intensity dramatically affects the reconstruction results. There are a number of factors that may influence the image intensity. We here review some typical ill-factors.

- Noise. Noise may be one of the most common ill-factors in a variety of imaging devices, including SEM. Noise makes the image intensity from multiple scans at a given position (pixel) be different. It is generally be modeled as a Gaussian distribution. As shown in Fig. 1.2 (b), the intensity profile of the center section of the sphere pattern does display smooth but randomly oscillating.

- Shadowing. Shadowing phenomena can frequently occur in imaging processes owing to the exceptional features of sample topography. As shown in Fig. 1.3, a portion of the electrons below the tangent line is screened out because of the occlusion, causing fewer electrons to be collected by the BSE detector, which consequently gives rise to smaller observed image intensity than the underlying shadowless one.

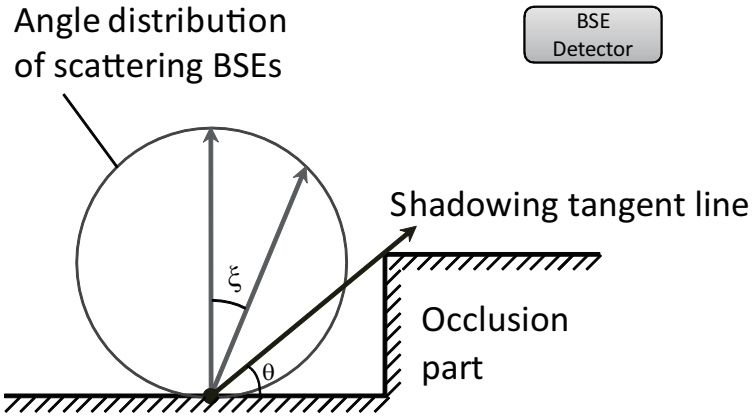

Figure 1.3: Schematic illustration of shadowing effect. BSEs emitted in a direction below the tangent line are generally absorbed by the occlusion region and consequently are not collected by the detector.

One can imagine that shadowing effects can contribute significantly to the final error of a reconstructed 3D surface

- Charging. Charging is the condition when a material cannot effectively conduct the beam energy imparted to it. A large fraction of the probe current remains in the specimen as the beam electrons lose all of their initial energy and are captured by the specimen. This charge flows to ground if the specimen is a conductor and a suitable connection exists. If the ground path is broken, even a conducting specimen quickly accumulate charge. The ensuing image will grow or cause streaks or general distortion in the image as electron production is artificially enhanced and the beam is unintentionally deflected.

- Blurring. Blurring occurs on account of out of focus leading the lose of image details. Imaging that an inclined flat specimen will make it difficult to be focused over the whole area, although the depth of focus of SEM is relatively large in general.

Among these ill-factors, noise and shadowing are generally unavoidable, because they are almost inherent in imaging processes. In particular, shadowing effect is caused by the exceptional features of specimen topography itself, which is considerably hard to avoid or eliminated. Moreover, as shown in Fig. 1.4 (c), it generally give rise to significant distortions to the final reconstructed shape. Nevertheless, charing problem can be relieved via specimen coating so as to increase the conductivity. Blurring may be resolved through such as dynamic focusing [32], where the focal length being changed during the scanning process.

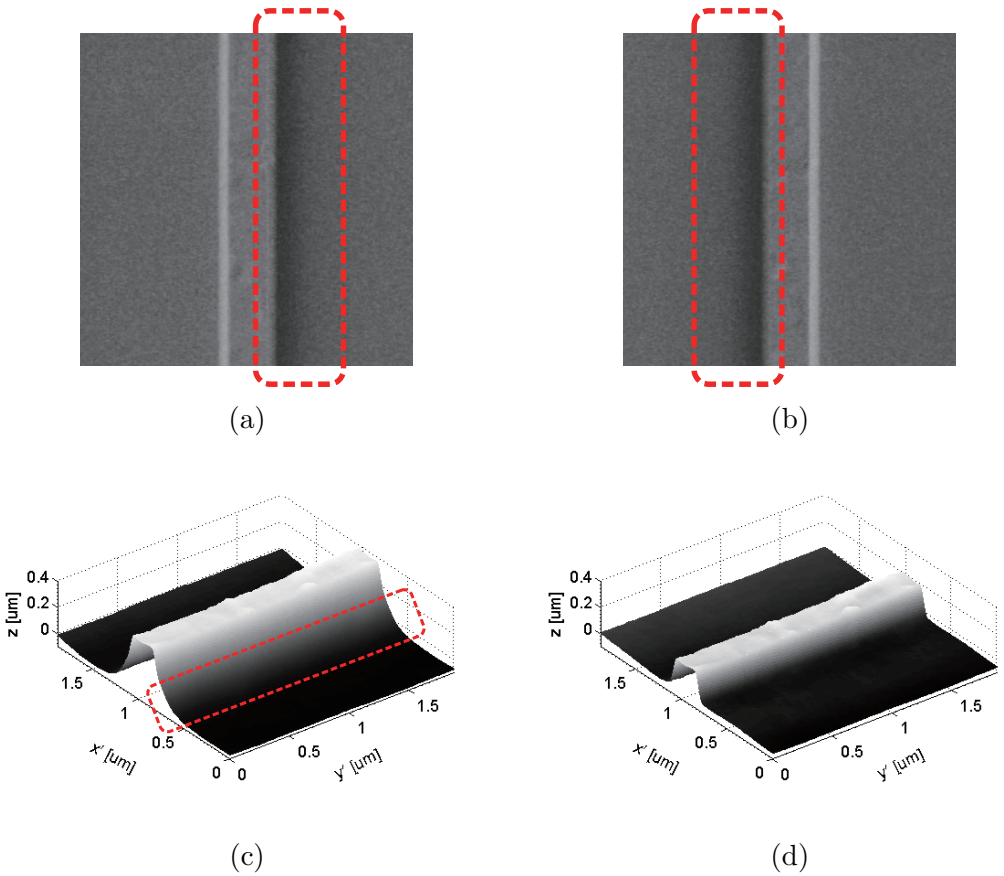

Figure 1.4: Shadowing effects in a line pattern: (a) original left image, (b) original right image, (c) reconstructed shape via the proposed variational method without de-shadowing, and (d) reconstructed shape via our proposed method with de-shadowing.

1.3 Scope of Our Work

Robustness is essential for real applications. In this work, we aim to develop a highly robust and automatic SEM photometric stereo. Our main focus is on noise and shadowing effects. In particular, the majority work is devoted to handling shadow problem.

1.3.1 Dealing with Noise

As discussed in the previous section, noise is almost inherent in the imaging processes, which gives rise to contamination to gradient estimations. In almost all the previous SEM photometric stereo studies, an numerical integration method was adopted to obtain the 3D shape from gradients. Such method is very simple, however, it has a drawback in that it performs poorly when the data are noisy, as the error can accumulate during the integration. A remedy is to reduce the level of noise, for instance, by averaging multiple images from the same static "scene" over time. However, it is generally expensive to

obtain the large number of images required for this process.

In contrast to acquire less noisy data, we alternatively pursue to allow a reconstruction algorithm to deal with noise issue. To this end, we implement an optimization technique, named variational method, to find the best-fit shape through minimization of the proposed energy functional. The functional is consist of two terms. One is the fidelity term that is to guarantee the gradient of reconstructed shape should be consistent with the gradient data. The second term is total variation regularizer to penalize the roughness of the solution and consequently make our method be robust to noise influence arising in the data term. In a statistical point of view, the minimization of the functional is equivalent to a maximum a-posteriori, where the fidelity term and TV regularizer are corresponding to likelihood and prior, respectively. We minimize the variational problem by solving the corresponding Euler-Lagrange equation, which is a partial differential equation (PDE). We resolve the PDE by first discretizing it through the finite difference method and adopting a fixed point method to solve the resulted Quasi-linear system after the discretization. Fig. 1.2 (c) and (d) are the reconstructed 3D shape of a sphere pattern via traditional integration method and our proposed variational method, respectively. It is vivid that 3D shape via our proposed method is considerably smooth and reliable, while significant distortions exist in the 3D shape via the integration method, which indicates that the proposed method can handling noise issue well compared to the integration method that is sensitive to noise effect.

1.3.2 Dealing with Shadowing

Fig. 1.4 (c) shows the reconstruction result of a line pattern via our proposed variational method. We can clearly observe that the marked region contains large deviation which display as rounding slope effects. Such error is in fact caused by shadowing effects, which can not been simply eliminated by the variational method.

Paluszyński and Slówko [11] introduced several techniques for reconstructing the shape in the shadowed region that utilize two or three unshadowed detectors under a setting of four secondary electron (SE) detectors. However, this method requires exact geometric parameters for the detector system, which are generally difficult to obtain. In addition, shadowed regions must be manually identified from the SE images each time. Such interactivity bring several shortcomings. Firstly, it is generally difficult to segment out the shadowed region precisely. As shown in Fig. 1.4 (a) and (b), it is difficult is determine the boundary between shadowed and non-shadowed regions. Secondly, the reproducibility of the results can hardly be guaranteed. Thirdly, the interactive implementation is generally time-consuming and restrictive for some actual applications.

In this work, we aim to a explore an algorithm that can automatically eliminate shadowing effects. To deal with shadowing effects, we need mathematically model the shadowing generation process. Unlike the noise effect, the modeling of shadowing ef-

fects needs a bit more elaboration. We thus introduce a novel shadowing compensation model, which is deduced by modeling image intensities in both cases of absence and presence of shadowing based on the angle distribution of signal electrons. In chapter 3, we deduce our first shadowing compensation model with a restrictive assumption that the shadowing effects occurs only on the horizontal surface. Benefit from such assumption, the shadowing compensation model gets a lot simplification and takes a compact and implicit form, that is convenient for applications. For instance, the assumed situation is generally common for measuring man-made structures such as semiconductors, whose height or shape need to be controlled precisely in manufacturing processes. We further make an extension to the model in chapter 5 where the restrictive assumption is abandoned and derive a general model called extended shadowing compensation model. The shadowing compensation model related the underlying shadowless image intensity to the observed one via detection ratio, which provides an essential cue to infer shadowless images. One advantage of the shadowing compensation model is that it is no need for us to treat the regions with shadowing errors separately from those without such errors, because the shadowless case is special case of shadowing with detection ratio being one. This does not require an image segmentation process to extract shadowing regions, which is substantially difficult to implement automatically.

With the shadowing compensation model, our proposed robust SEM photometric stereo is finally formulated as a constrained variational problem. In the fidelity term of the objective functional, the gradient data is evaluated from the underlying shadowless images, and the shadowless images are related to the observed ones via our shadowing compensation model which forms the constraints. We adopt an iterative scheme to solve the problem, which performs commutatively between the compensation of image intensities and the modification of the corresponding 3D shape, can effectively provide both an accurate 3D shape and compensated shadowless images after convergence. Fig. 1.4 (d) shows the reconstructed 3D shape of the line pattern which indicate that our proposed SEM photometric stereo is robust to noise and shadowing effects in an automatic and effective way.

1.4 Advantages and Contributions

The advantages of the proposed robust SEM photometric stereo are summarized as follows:

- Robustness. Surprisingly, the previous SEM photometric stereo research studies have exploited robustness to a very limited extent. In this work, we focus on two ill-factors, i.e., noise and shadowing effects, because both are almost inherently occur in imaging processes. In particular, the shadowing effects is caused by the specimen itself and thus impossible be avoided once exists. Utilizing our shadowing compensation model and variational method, the SEM photometric stereo can simultaneously deal with the both issues.

- Shadowless Images. One interesting advantage of our method is that we obtain not only 3D shape, but shadowless images. As previously mentioned, shadowing effects, once exists, can hardly be avoided. Therefore, it is difficult to directly obtain the shadowless images in SEM. Our method provides a potential opportunity for improving the imaging performance of SEM devices.

- Full-automatic. In contrast to a literature example [11], there is no human interactivity required in the reconstruction and de-shadowing process. This is benefit from our shadowing compensation model where the shadowless case is just a special condition of shadowing.

This thesis has several novel contributions which are summarized as follows:

- Validation the gradient equation. We analyze the applicability of the gradient equation via an experimental validation, as the equation is not theoretically deduced but experimentally found.

- Shadowing Compensation Model. We model the shadowing generation process and introduce a novel shadowing compensation model by modeling the image intensities in both cases of absence and presence of shadowing. The model related the underlying shadowless image intensity to the observed one and provide a essential cue for de-shadowing.

- Reconstruction with De-shadowing. The formulated our reconstruction as a constrained variational problem. We also propose an efficient numerical solution to the problem, which can produce a 3D shape and shadowless images.

- Extended Shadowing Compensation Model. We extended the shadowing compensation model from the horizontal case to general inclined cases. The model tends to be more applicable and has a higher model accuracy when applied to a shadowed region with a large inclination.

1.5 Organization of the Thesis

In this chapter, we have briefly described the imaging process in SEM and the overview of previous studies in the fields of SEM 3D reconstruction. We have highlighted the typical problems and difficulties in SEM photometric stereo. We have also briefly described the concepts of our proposed robust SEM photometric stereo. The remainder of the thesis is organized as follows:

- Chapter 2 briefly describes the measuring system for SEM photometric stereo and gradient estimation equation. We also design an experiment for the validation of the equation, as the equation is experimental found.

- Chapter 3 introduces the shadowing compensation model. Our modeling is divided into two steps. We firstly model the image intensities in both cases of absence and presence of shadowing under some ideal assumptions and deduce the primary model. We further incorporate the practical factor into the model and derive the final modified model.

- Chapter 4 presents our proposed SEM photometric stereo. In this chapter, we utilize the shadowing compensation model and formulate our robust reconstruction through a variational method, which can robust against noise and shadowing effects. We further propose the numerical implementation for minimizing the problem. At the end of the chapter, we present several experiments on real image data with different conditions of shadowing as well as noise.

- Chapter 5 extends the shadowing compensation model to a more general one. In this chapter, we abandoned the previous restrictive assumptions and extend the model to general curved surfaces. We also present a numerical method for solve the extend model. Finally we evaluate the performance of the extended model by comparisons with the previous model and absence of de-shadowing cases under different shadowing conditions.

- Chapter 6 concludes the main points of our work and discusses the future works.

Chapter 2. Gradient Estimation

This chapter briefly describes our measuring system and the gradient estimation equation. As the gradient equation is experimentally found, we therefore design an experiment to validate the effectiveness of the equation in our system setting. The basic idea is to check whether the gradients estimated by the equation are kept unchanged on the locus with an identical gradient. We realize that measurements are influenced by noise and the hypothesis can not hold exactly. We thus present an method to estimate the noise level from just a single image and estimate the standard deviation of the gradient measurements caused by image noise.

2.1 Gradient Estimation Equation

The SEM photometric stereo method is substantially related to the photometric techniques used with an optical camera as measuring device [15, 16, 17] in that both are used to estimate gradient information for an object being observed from shading cues in the image data (The special case, in which the data is a single image, is generally known as shape from shading [18, 19, 20, 54, 55, 56]). However, because of different imaging principles, the gradient estimation formulas are derived in different ways.

As schematically illustrated in Fig. 2.1 [7], in our SEM measurement system, two BSE detectors are symmetrically positioned along a direction. It is convenient for us to define this direction as an x-axis. Such a system can simultaneously provide two BSE images from the two detectors, denoted as BL and BR, respectively. In general, we use

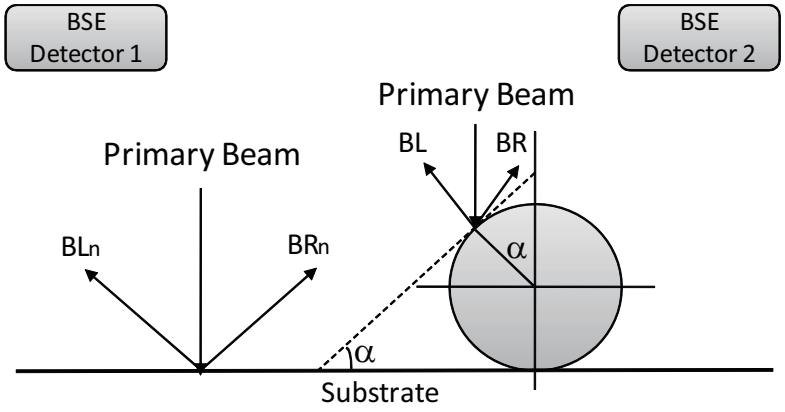

Figure 2.1: Schematic diagram of measuring system with two BSE detectors.

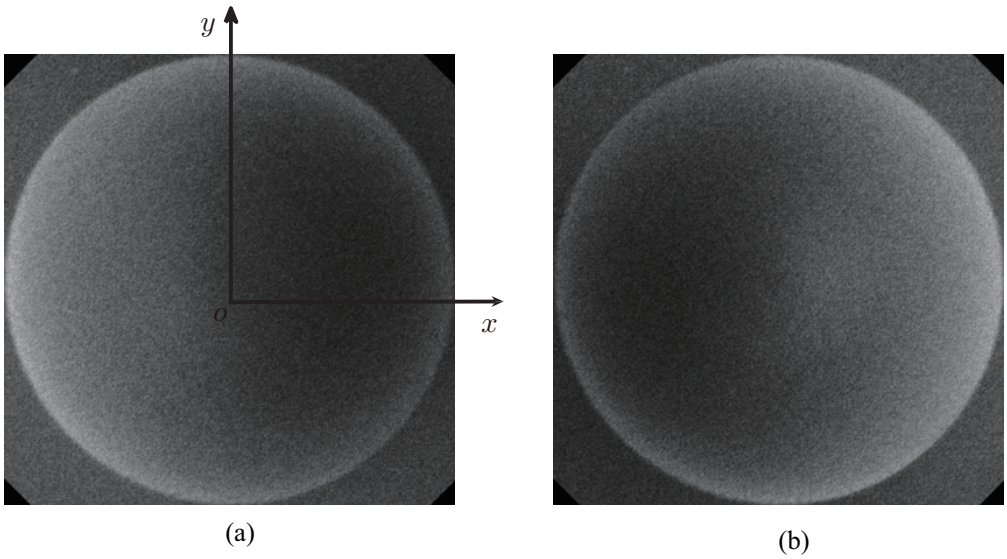

Figure 2.2: Image coordinate shown on the left image (a) of the sphere pattern. (b) Right image of the sphere pattern.

BL and BR to refer to the left and right image and detector 1 and 2 to designate the left and right detector, respectively. Suganuma [7] proposed an experimentally derived equation that could measure the gradient component in the direction of the x-axis (i.e., the slope $\tan\alpha$):

$$\frac{\partial Z}{\partial x} = k\frac{\mathrm{BL}^2 - \mathrm{BR}^2}{(\mathrm{BL_n} + \mathrm{BR_n})^2}, \tag{2.1}$$

where k is a constant and $\mathrm{BL_n}$ and $\mathrm{BR_n}$ are signal outputs from two detectors on the horizontal specimen surface. 3D shape can be obtained from gradient measurements though either straightforward numerical integration [7] or advanced optimization techniques [14, 30, 13].

2.2 Experimental Validation

As Suganuma's equation (2.1) is experimentally derived, we thus design an experiment to validate the accuracy and effectiveness. To this end, we choose a sphere pattern, and check whether value $\mathrm{G} = \mathrm{BL}^2 - \mathrm{BR}^2$ keeps a constant for the positions on the sphere with a identical gradient. Here we utilize numerator $\mathrm{G} = \mathrm{BL}^2 - \mathrm{BR}^2$ instead of the whole right hand side of (2.1) for computational efficiency, because both parameter k and denominator $(\mathrm{BL_n} + \mathrm{BR_n})^2$ are kept unchanged in each individual measurement. There are two considerations for the choice of the sphere pattern in our experiment. For one thing, the 3D shape of the sphere can easily be constructed making the ground truth of gradients be effortlessly obtained. For another, the sphere contains all the cases of inclination leading the validation be more reasonable and reliable. Because the measurements (BL and BR) are inevitably contaminated by noise in our experiments, the

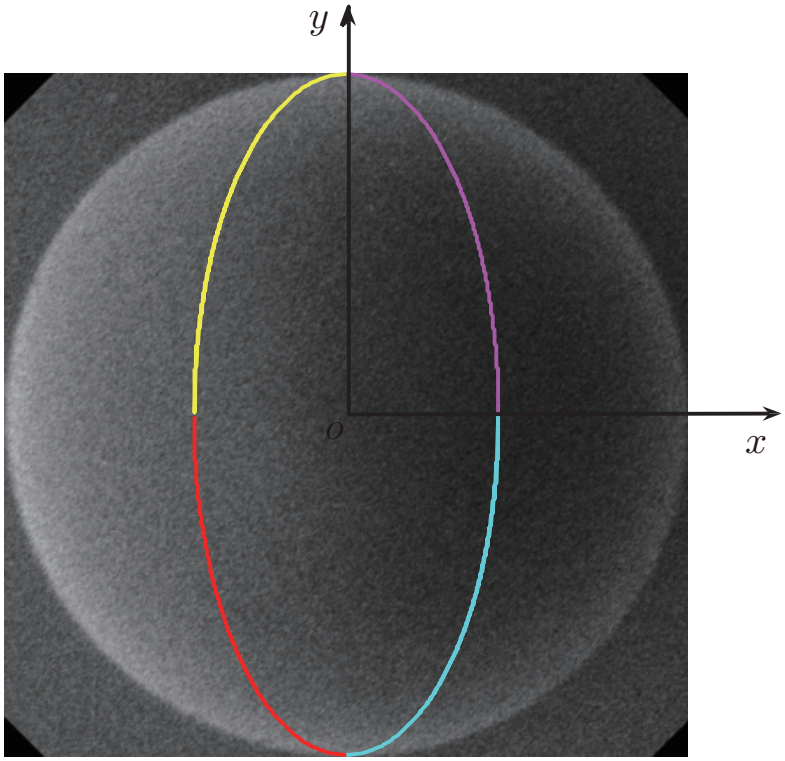

Figure 2.3: Locus with $C = 0.5$ shown on the left image.

hypothesis that G remains constantly can never hold exactly in practice. Therefore, we have to take the noise influence into consideration. We thus present an estimation of noise level in images and the corresponding error in G caused by noise.

2.2.1 Locus with Identical Gradient

Left and right images of the sphere pattern are shown in Fig. 2.2. The images are rotated and truncated from original images (refer also to Fig. 2.5 (a) and Fig. 2.6 (a)) so that the image coordinate is coincident to horizontal and vertical directions and the origin is at the center of the sphere.

The shape of the sphere pattern takes

$$Z = \sqrt{r^2 - x^2 - y^2}, \tag{2.2}$$

where r is the radius of the sphere which is 193 (in pixel) in our experiment. It is thus straightforward that the gradient is

$$\frac{\partial Z}{\partial x} = -\frac{x}{\sqrt{r^2 - x^2 - y^2}}. \tag{2.3}$$

The locus of the points with the same absolute gradient value C (where $C \geq 0$), i.e.,

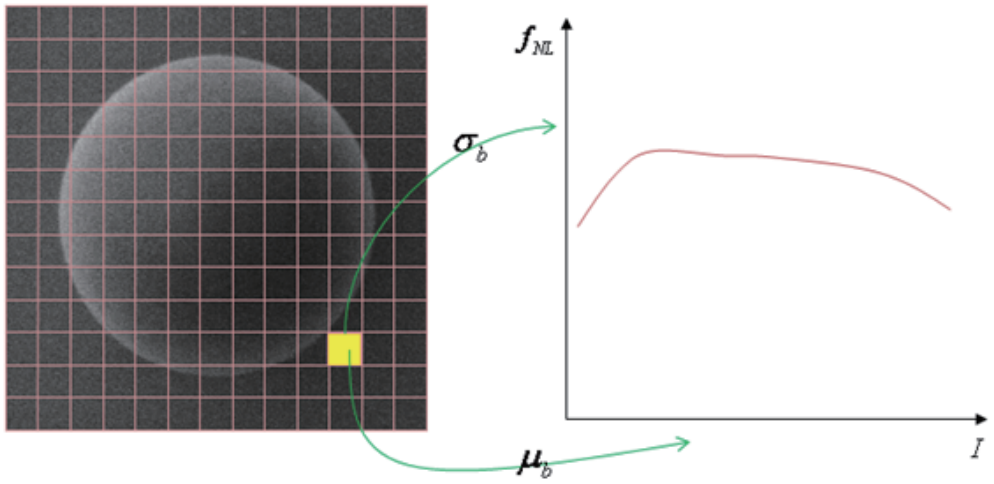

Figure 2.4: Mean and standard deviation of image blocks constitute the noise level function.

$|\frac{\partial Z}{\partial x}| = C$, should satisfy

$$y = \pm\sqrt{r^2 - x^2\left(1 + \frac{1}{C^2}\right)}, \tag{2.4}$$

or equivalently

$$x = \pm\sqrt{\frac{r^2 - y^2}{1 + 1/C^2}}. \tag{2.5}$$

Fig. 2.3 shows the locus in the four quadrants with $C = 0.5$.

2.2.2 Noise Level Estimation

In this section, we present the estimation of noise level from a single image (BL or BR), which is further used for the estimation of error in G caused by noise.

Noise Model

We take the following additive noise model

$$I(i,j) = \bar{I}(i,j) + n(i,j), \tag{2.6}$$

where I denotes the observed noise image, $\bar{I}$ is the underlying noise-free image, n is random variable denoting noise, and i and j denote row and column indices of image pixels, respectively.

Assumptions

Noise at each pixel is independent and identically from a gaussian distribution with expectation zero. Such assumption implies

- $\varepsilon\{n(i,j)\} = 0$ for all (i,j), i.e. $\bar{I} = \varepsilon\{I\}$.
- $\varepsilon\{n(k,l) + n(p,q)\} = \varepsilon\{n(k,l)\} + \varepsilon\{n(p,q)\}$ for $(k,l) \neq (p,q)$.
- $\varepsilon\{n(k,l) \cdot n(p,q)\} = \varepsilon\{n(k,l)\} \cdot \varepsilon\{n(p,q)\}$ for $(k,l) \neq (p,q)$.

Where $\varepsilon\{\cdot\}$ denotes the expectation operator.

Estimation of Noise Level Function

since there is no prior knowledge about noise, we have to estimate the noise level from a single image. To this end, we define the following noise level function

$$f_{NL} = \sqrt{\varepsilon\{n^2\}} = \sqrt{\varepsilon\{(I - \bar{I})^2\}}. \tag{2.7}$$

With the previous assumption, we have $\bar{I} = \varepsilon\{I\}$.

As illustrated in Fig. 2.4, the procedure for estimation of the noise function f_{NL} is as follows:

- Noise image I is divided into blocks of size $N \times N$.
- For each block, the mean and standard deviation are calculated via

$$\mu_b = \frac{1}{N^2} \Sigma_{I(i,j) \in \text{block}} I(i,j),$$

$$\sigma_b = \sqrt{\frac{1}{N^2 - 1} \Sigma_{I(i,j) \in \text{block}} (I(i,j) - \mu_b)^2}.$$

Where the subscript b implies block.

Experimental Estimation Results

The experiments are implemented on the original left and right images. Fig. 2.5 and 2.6 show the estimation results with block size being 4×4, 8×8 and 16×16. As we can observe, the standard deviations for all the block sizes are around 10 and the functions are very near to a uniform distribution. Therefore, as a reasonable approximation, we calculate the standard derivation for each block size by averaging f_{NL}. Table 2.1 shows averaged standard deviations of left and right images. We further observe that standard deviation for both images are quite close to each other. We thus take the average of the both average over different sizes as the noise level in images. The estimated noise level $\sigma = \frac{10.5508 + 10.8757}{2} = 10.7133$.

Table 2.1: Standard deviations of left and right images

	$N = 4$	$N = 8$	$N = 16$	Average
Left image	9.9665	10.5312	11.1548	10.5508
Right image	10.2168	10.8321	11.5783	10.8757

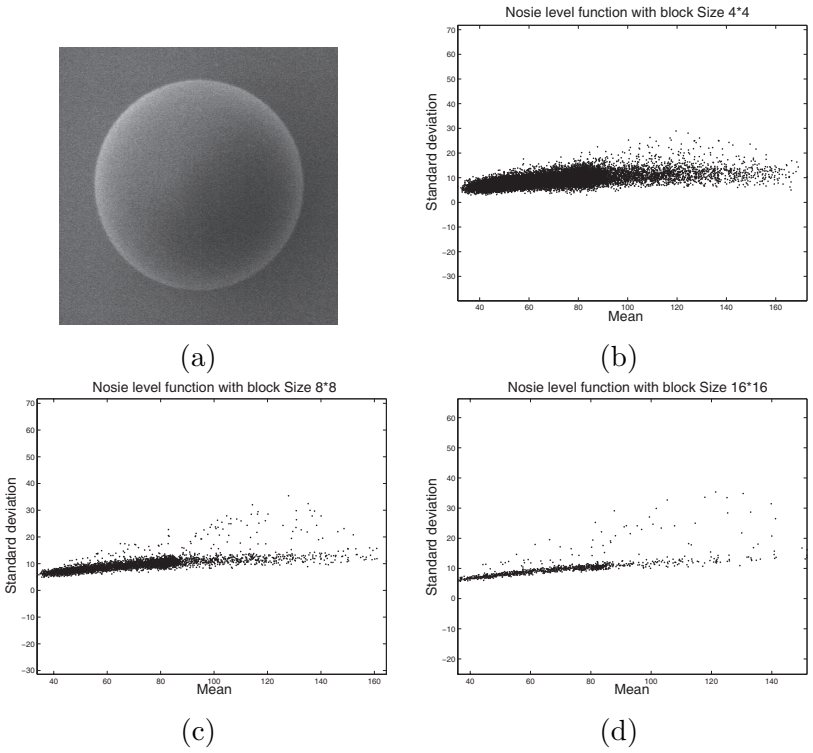

Figure 2.5: Noise level function of the left image BL (a) with different block sizes. (b) size 4×4, (c) size 8×8 and (d) size 16×16.

2.2.3 Error in G Caused by Noise

In this section, we deduce the standard deviation of $\mathrm{G} = \mathrm{BL}^2 - \mathrm{BR}^2$, i.e., expectation of error caused by image noise. According to the previous noise model,

$$\mathrm{BL} = \overline{\mathrm{BL}} + n_1,$$

$$\mathrm{BR} = \overline{\mathrm{BR}} + n_2,$$

where BL and BR denote observed left and right images, respectively, $\overline{\mathrm{BL}}$ and $\overline{\mathrm{BR}}$ represent noise-free images and n_1,n_2 denote noise. The measurement of G we observe is $\mathrm{G} = \mathrm{BL}^2 - \mathrm{BR}^2$, while the underlying noise-free one should be $\bar{\mathrm{G}} = \overline{\mathrm{BL}}^2 - \overline{\mathrm{BR}}^2$. The

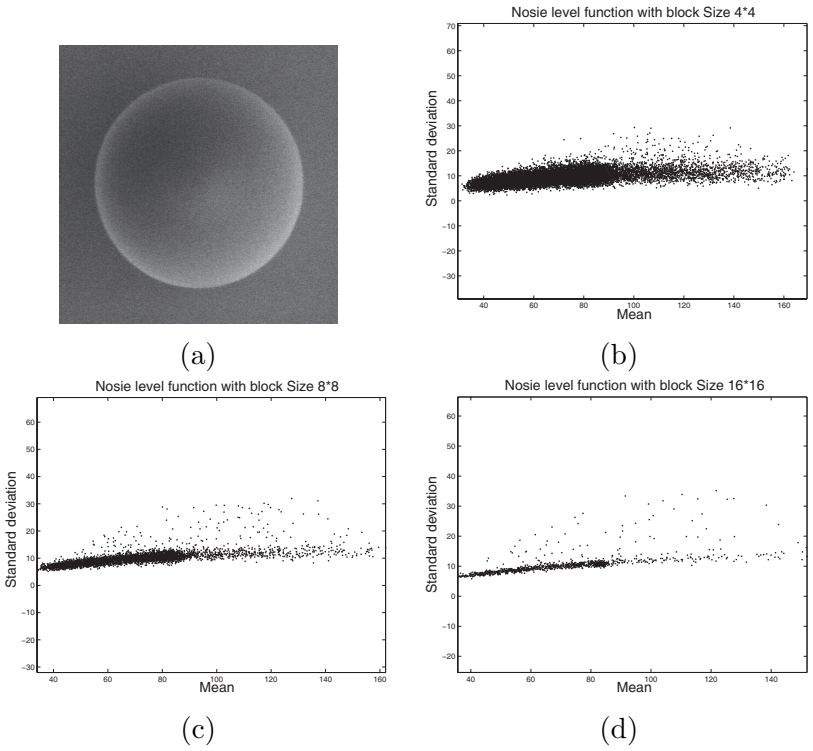

Figure 2.6: Noise level function of the right image BL (a) with different block sizes. (b) size 4×4, (c) size 8×8 and (d) size 16×16.

the standard deviation of $\mathrm{G} = \mathrm{BL}^2 - \mathrm{BR}^2$ can be estimated as follows:

$$\begin{aligned}
\sigma(\mathrm{G}) = \varepsilon\left\{\left|\mathrm{G} - \bar{\mathrm{G}}\right|\right\} &= \varepsilon\left\{\left|(\mathrm{BL}^2 - \mathrm{BR}^2) - (\overline{\mathrm{BL}}^2 - \overline{\mathrm{BR}}^2)\right|\right\} \\
&= \varepsilon\left\{\left|n_1^2 - n_2^2 + 2\overline{\mathrm{BL}} \cdot n_1 - 2\overline{\mathrm{BR}} \cdot n_2\right|\right\} \\
&= \varepsilon\left\{\left|2\overline{\mathrm{BL}} \cdot n_1 - 2\overline{\mathrm{BR}} \cdot n_2\right|\right\} = 2\varepsilon\left\{\sqrt{\left(\overline{\mathrm{BL}} \cdot n_1 - \overline{\mathrm{BR}} \cdot n_2\right)^2}\right\} \\
&= 2\varepsilon\left\{\sqrt{\overline{\mathrm{BL}}^2 \cdot n_1^2 + \overline{\mathrm{BR}}^2 \cdot n_2^2 - 2\overline{\mathrm{BL}}\ \overline{\mathrm{BR}} \cdot n_1 \cdot n_2}\right\} \\
&= 2\sigma\varepsilon\left\{\sqrt{\overline{\mathrm{BL}}^2 + \overline{\mathrm{BR}}^2}\right\} \\
&= 2\sigma\sqrt{\varepsilon\left\{\mathrm{BL}\right\}^2 + \varepsilon\left\{\mathrm{BR}\right\}^2}
\end{aligned} \tag{2.8}$$

Here we have employed the assumption that $\varepsilon\{n_1^2\} = \varepsilon\{n_2^2\}$, $\varepsilon\{n_1 \cdot n_2\} = \varepsilon\{n_1\} \cdot \varepsilon\{n_2\} = 0$ and $\overline{\mathrm{BL}} = \varepsilon\left\{\mathrm{BL}\right\}$, $\overline{\mathrm{BR}} = \varepsilon\left\{\mathrm{BR}\right\}$. σ is the standard deviation of image noise that has been estimated in the previous section.

2.2.4 Experimental Validation Results

In this section, we provide the numerical validation results. The idea is to check whether the values of $\mathrm{G} = \mathrm{BL}^2 - \mathrm{BR}^2$ keep unchanged on the locus with a identical

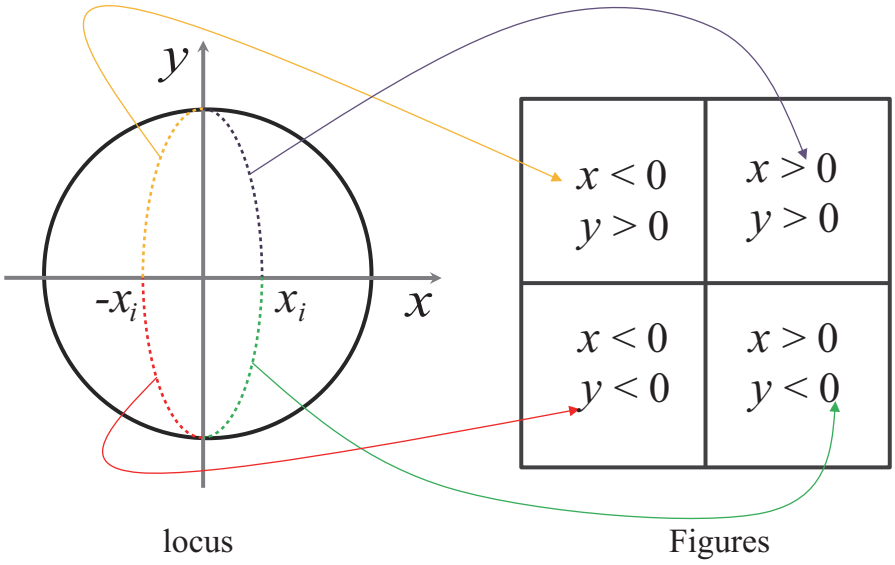

Figure 2.7: Plot arrangement.

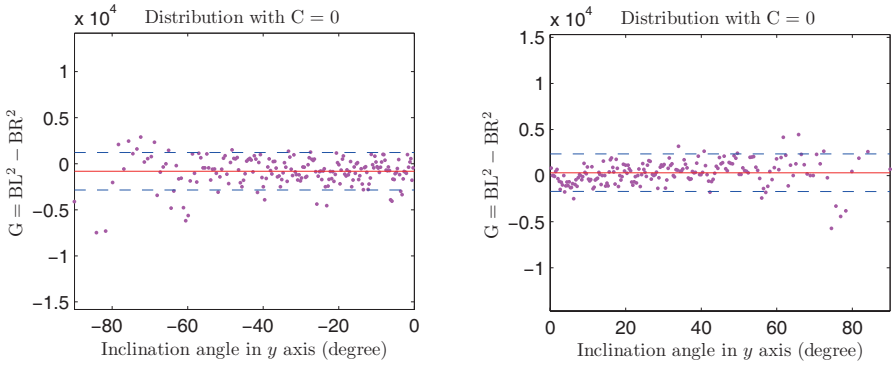

Figure 2.8: Distribution of G with $x_i = 0$.

gradient C. As previously mentioned, on account of noise influence, the hypothesis can not strictly hold. We thus design the experiment as follows,

- Find the locus with $C = \frac{\partial Z}{\partial x_i}$, where x_i is the sampling point along x-axis.
- For each locus, check whether G evaluated on all the points mainly located in the range $[\bar{\mathrm{G}} - \sigma(\mathrm{G}),\ \bar{\mathrm{G}} + \sigma(\mathrm{G})]$.

We check the locus in the four quadrants, and the plot layout is illustrated in Fig. 2.7. Fig. 2.9 - 2.13 show the plots with $\{x_i|1,\ 10,\ 20,\ \cdot,\ 140,\ 150\}$ with a sampling step 10 (in pixel). As we can observe, the majority of the points are with the range $[\bar{\mathrm{G}} - \sigma(\mathrm{G}),\ \bar{\mathrm{G}} + \sigma(\mathrm{G})]$, which indicates that the Suganuma's equation can hold well under our experiment settings.

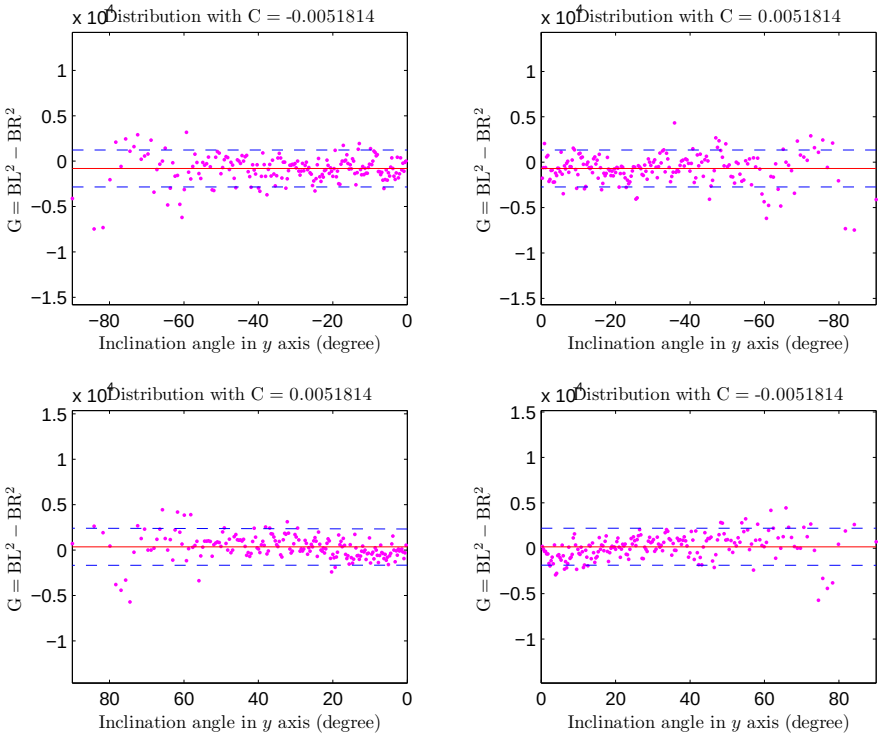

Figure 2.9: Distribution of G with $x_i = 1$.

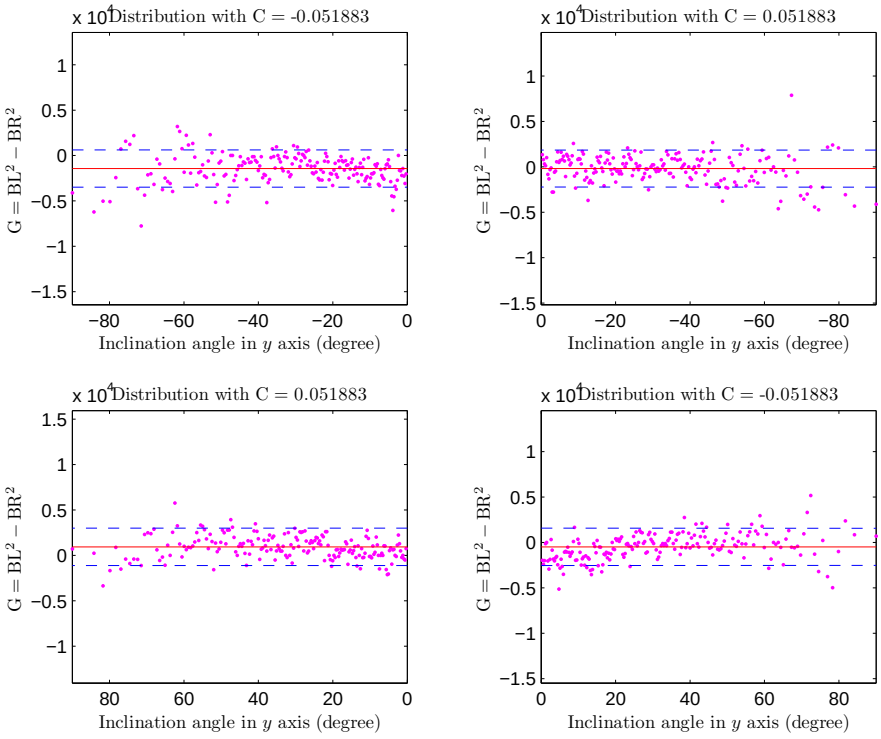

Figure 2.10: Distribution of G with $x_i = 10$.

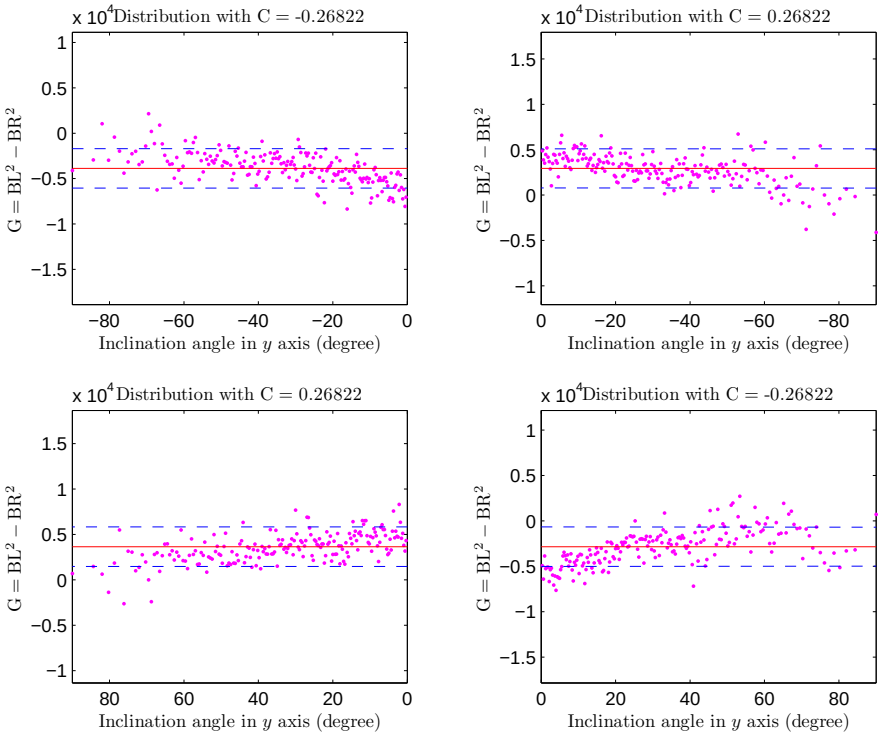

Figure 2.11: Distribution of G with $x_i = 50$.

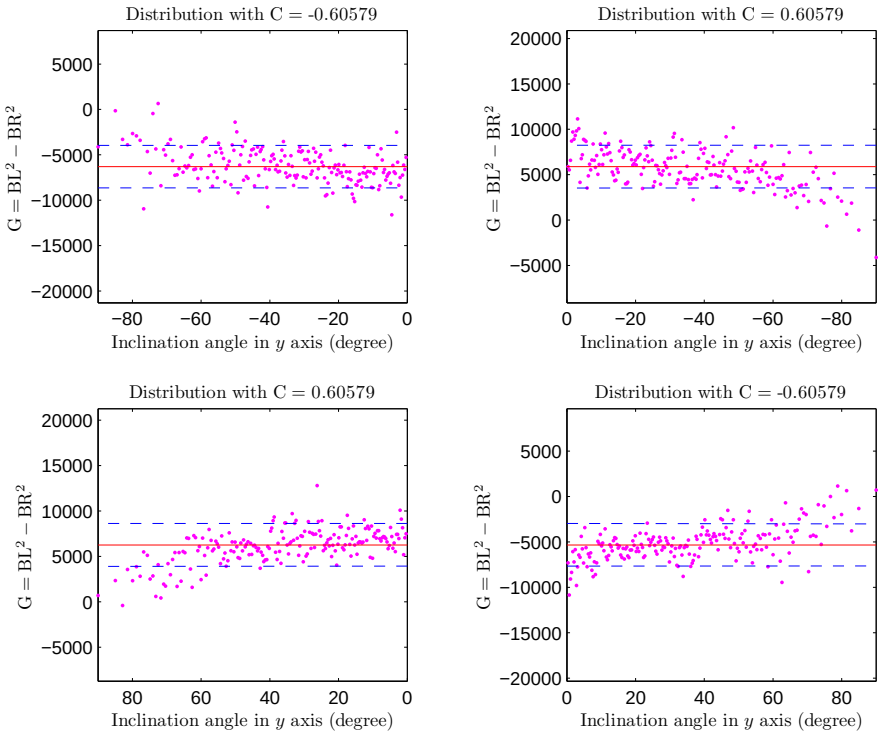

Figure 2.12: Distribution of G with $x_i = 100$.

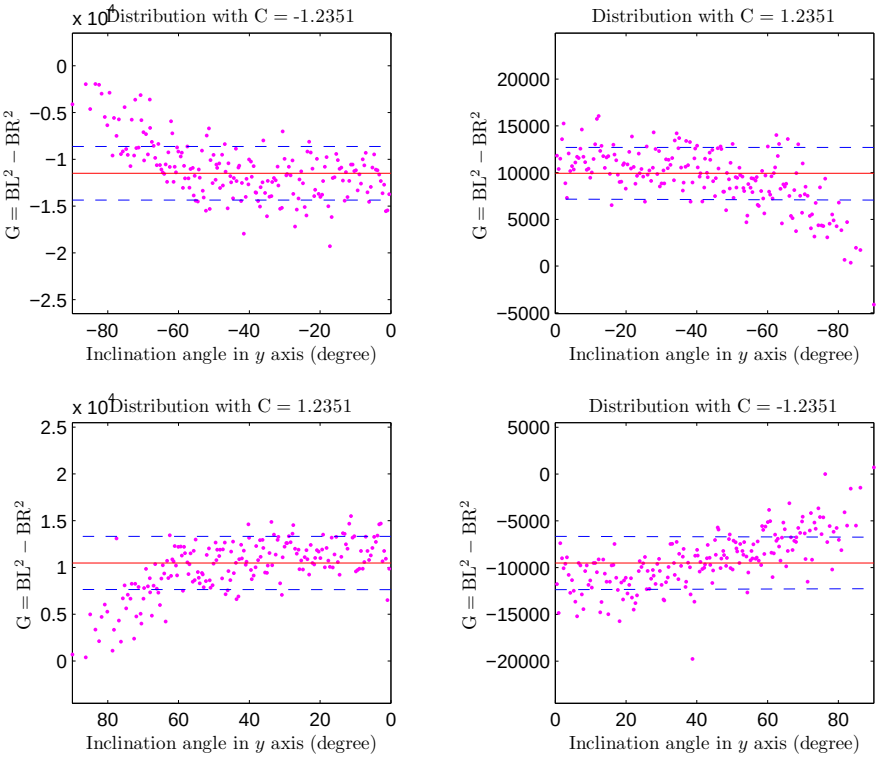

Figure 2.13: Distribution of G with $x_i = 150$.

2.3 Conclusion Remarks

In this chapter, we have numerically validated the effectiveness of Sugunama's equation in our system setting. Suganuma's fitting model (2.1) can be effective provided the image intensities of both BL and BR are reliable.

It is obvious that the accuracy of gradient greatly influence the reconstruction results in SEM photometric stereo. However, practical measurements of image intensity are generally influenced by numerous ill-factors, including shadowing and noise effects. It is thus that the reconstructed 3D shape contains significant distortion when the gradient measurements are inaccurate that is generally on account of ill-factors.

As previously shown in Fig. 1.2 and Fig. 1.4, it is a vivid comparison between the traditional and proposed reconstruction results. In particular, the shadowing effects gives significant distortions in the reconstructed shape. As we can observe in Fig. 1.4, both left and right images contain shadowing effects in the marked regions. Such shadowing effects give rise to significant distortions in the reconstructed shape as marked in Fig. 1.4 (c). As a motivation of the following chapters, our proposed SEM photometric stereo method seeks to be robust against noise effects and eliminate shadowing errors automatically so as to achieve a high accurate reconstruction.

2.3.1 Overview of Proposed SEM Photometric Stereo

For dealing with shadowing errors as well as noise effects, we develop the robust photometric stereo method by applying the following general ideas.

(1) **Shadowing Compensation Model**
For eliminating shadowing errors, it is necessary to model the mechanism of generation of shadowing effects. To this end, we considered the angle distribution of backscattered electrons (BSEs) as a modified Lambert's cosine law. Using the angle distribution of BSEs, we explore how the BSE intensity (signal output) with shadowing errors is related to the underlying BSE intensity without shadowing errors. As a result, a shadowing compensation model is introduced, that can derive shadowless BSE intensities from shadowed measurements provided that the corresponding shadowing angles are known. The shadowing compensation model is further modified by updating the BSE detection model. Three practical factors in the BSE detection process are in turn considered and further modeled by incorporating the corresponding three parameters, with which the accuracy and flexibility of the shadowing compensation model can be improved.

(2) **Estimating the 3D Surface and Shadowless Images**
With a true 3D surface, we can calculate the shadowing angles and derive the underlying shadowless images from the original measured shadowed images using the shadowing compensation model. On the other hand, if shadowless images are provided, gradient measurements derived via Suganuma's equation could be accurate enough to estimate a reliable 3D surface. However, both these situations are the targets we are striving toward, and the problem essentially boils down to something such as a "chicken-and-egg" dilemma. We propose an iterative solution to the problem, that operates commutatively between shadowing compensation of the BSE images using the shadowing compensation model and reconstruction of the 3D surface from the compensated BSE images based on Suganuma's equation for calculating the gradient and a proposed noise-robust regularization optimization method for estimating depth from the gradient. After convergence of the iterative process, both a reliable 3D surface and shadowless images are provided.

Chapter 3. Shadowing Compensation Model

In the chapter, we introduce a novel shadowing compensation model (SCM) for mathematically modeling the shadowing effects. The derivation of SCM is divided into two steps. In the first step, for the convenience of the modeling, we deduce a primary model with some temporary assumptions, though modeling the image intensities in both cases of absence and presence of shadowing effects. In the second step, we modified the model by incorporating certain practical factors.

3.1 Assumptions

We introduce the shadowing compensation model under the following two assumptions:

1. The BSE image intensity is proportional to the amount of backscattered electrons (BSEs) collected by the detector.

2. The angle distribution of BSEs can be expressed as follows:

$$\frac{d\eta}{d\omega} = \frac{\eta_0}{\pi} \cos^n \xi, \tag{3.1}$$

   where ξ describes the angle between the surface normal and the direction of the electron emission; η_0 is a coefficient; η and ω denote the quantity of BSEs and the solid angle, respectively; and the parameter n ensures more flexibility while describing the angular distribution in terms of the Lambert's cosine law, in which the parameter is equal to one [12].

In the following discussion, we restrict our problem domain to a situation in which the shadowing effect exists only in the horizontal region, in part, because the situation is generally common for measuring man-made structures such as semiconductors, whose height or shape need to be controlled precisely in manufacturing processes. In such restricted situation, the shadowing compensation model can be derived in a closed form.

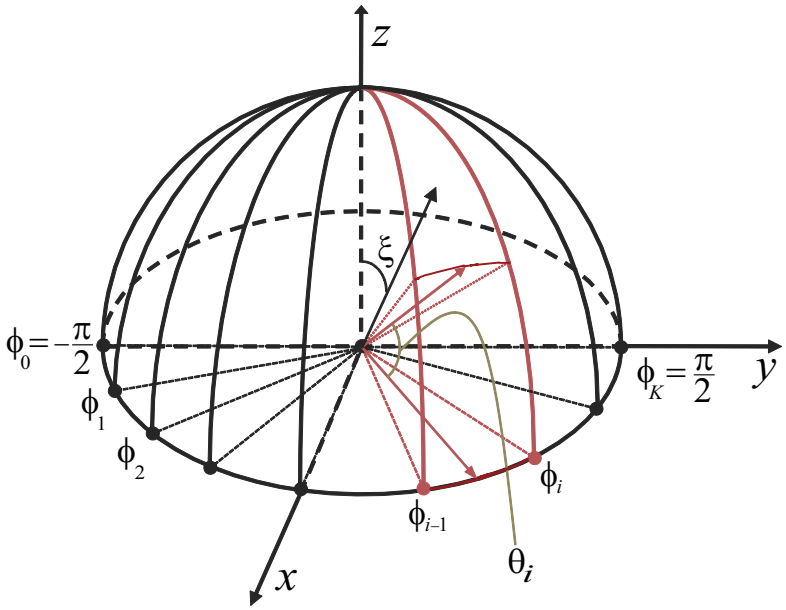

Figure 3.1: Detectable region of a BSE detector.

3.2 Primary SCM

3.2.1 BSE Intensity in the Absence of Shadowing

For convenience, we temporally assume the occlusion phenomena and detecting ability of the detectors are ideal, i.e., the BSEs below the shadowing tangent line are totally absorbed and all the unshadowed BSEs are collected by the corresponding detectors.

Based on the ideal detecting ability assumption on the detectors, in the case of no shadowing, a BSE detector (the right detector for consideration) ideally collects BSEs in a quarter sphere region,

$$\Omega : \begin{cases} -\frac{\pi}{2} \le \phi \le \frac{\pi}{2}, \\ 0 \le \xi \le \frac{\pi}{2}. \end{cases} \tag{3.2}$$

Here ϕ and ξ denote the azimuth and zenith angles, respectively (see Fig. 3.1). It is convenient for us to just assume the intensity of a single BSE image (left or right) at a point of observation reflects the amount of BSEs collected by the corresponding detector. Therefore, the BSE intensity without shadowing can be derived as follows:

$$\begin{aligned} \mathrm{BSE}_{\mathrm{shadowless}} &= \int_\Omega \frac{d\eta}{d\omega} d\omega = \int_\Omega \frac{\eta_0}{\pi} \cos^n \xi d\omega \\ &= \frac{\eta_0}{\pi} \int_{-\pi/2}^{\pi/2} d\phi \int_0^{\pi/2} \cos^n \xi \sin \xi d\xi \\ &= \frac{\eta_0}{n+1}. \end{aligned} \tag{3.3}$$

Here we employed the fact that $d\omega = \sin \xi d\phi d\xi$ in the calculation of the integral.

3.2.2 BSE Intensity in the Presence of Shadowing

In the shadowing case, the BSE detectable region should be Ω minus the occluded region. Without introducing a loss of generality, we assume that the right detector is shadowed (see Fig. 3.1). We denote such a detectable region under the shadowing condition as

$$\Omega^S : \begin{cases} -\frac{\pi}{2} \leq \phi \leq \frac{\pi}{2}, \\ 0 \leq \xi \leq \frac{\pi}{2} - \theta(\phi). \end{cases} \tag{3.4}$$

Here, $\theta(\phi)$ is the shadowing angle along the ϕ direction, which generally varies for different values of ϕ. Similar to the case with no shadowing, the intensity can be derived by

$$\begin{aligned} \text{BSE} &= \int_{\Omega^S} \frac{d\eta}{d\omega} d\omega = \int_{\Omega^S} \frac{\eta_0}{\pi} \cos^n \xi d\omega \\ &= \frac{\eta_0}{\pi} \int_{-\pi/2}^{\pi/2} d\phi \int_0^{\pi/2-\theta(\phi)} \cos^n \xi \sin \xi d\xi. \end{aligned} \tag{3.5}$$

A problem here, however, is that an analytical expression for $\theta(\phi)$ is unlikely to be accessible. This issue can be resolved by dividing the detectable region Ω^S into small segment regions:

$$\Omega^S = \bigcup_{i=1}^{K} \Omega_i^S, \tag{3.6}$$

where,

$$\Omega^S : \begin{cases} \phi_{i-1} \leq \phi \leq \phi_i, \\ 0 \leq \xi \leq \frac{\pi}{2} - \theta_i \end{cases} \tag{3.7}$$

It is reasonable to assume that the shadowing angle within each small region Ω_i^S remains approximately constant, that is, $\theta(\phi) \approx \theta_i$ for $\phi_{i-1} \leq \phi \leq \phi_i$, $1 \leq i \leq K$. Hence, we can calculate the BSE intensity under these circumstances as follows:

$$\begin{aligned} \text{BSE} &= \int_{\Omega^S} \frac{\eta_0}{\pi} \cos^n \xi d\omega = \sum_{i=1}^{K} \int_{\Omega_i^S} \frac{\eta_0}{\pi} \cos^n \xi d\omega \\ &= \frac{\eta_0}{\pi} \sum_{i=1}^{K} \int_{\phi_{i-1}}^{\phi_i} d\phi \int_0^{\pi/2-\theta(\phi)} \cos^n \xi \sin \xi d\xi \\ &\approx \frac{\eta_0}{\pi} \sum_{i=1}^{K} \int_{\phi_{i-1}}^{\phi_i} d\phi \int_0^{\pi/2-\theta_i} \cos^n \xi \sin \xi d\xi \\ &= \frac{\eta_0}{n+1} \cdot \sum_{i=1}^{K} \frac{1 - \sin^{n+1} \theta_i}{K}. \end{aligned} \tag{3.8}$$

In (3.8), it is obvious that the larger the segment K number, the greater the accuracy of the intensity value. Moreover, the derived intensity would achieve the actual value in the limiting case where $K \to +\infty$.

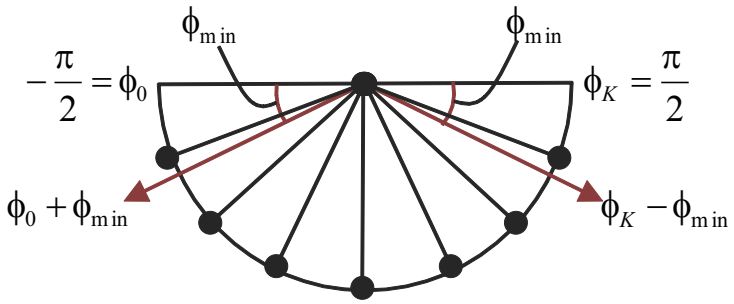

Figure 3.2: Geometric representations of practical factors $\phi_{\min}$.

3.2.3 Primary SCM

Equations (3.8) model the BSE intensity under the shadowing condition. In fact, the shadowless case can be considered as a special shadowing case in which all the shadowing angles are zero, which can be verified by setting $\theta_i = 0$ in Equations (3.8). Generalizing this observation, we can deduce the following primary SCM by combining (3.3) and (3.8).

$$\mathrm{BSE}_{\mathrm{shadowless}} = \mathrm{BSE} / \left(\sum_{i=1}^{K} \frac{1 - \sin^{n+1} \theta_i}{K} \right). \tag{3.9}$$

This model provides an important cue for estimating the underlying shadowless BSE intensity from an observed BSE intensity constrained by shadowing effects.

3.3 Improvements to SCM

In the previous section, we have derived the shadowing compensation model under the ideal setting on occlusion and detection of BSEs. To optimize the process for modeling shadowing effects, however, some practical factors must be considered.

3.3.1 Practical Modeling of Parameters

The Parameter $\phi_{\min}$

When calculating the BSE intensity using (3.3) and (3.8), in both case it was assumed that the range of ϕ was from $-\frac{\pi}{2}$ to $\frac{\pi}{2}$. Nonetheless, BSEs in the region where ϕ is near $\pm\frac{\pi}{2}$ generally cannot be detected owing to the practical limitations of the detector. To circumvent this shortfall, we introduce the parameter $\phi_{\min}$. As shown in Fig. 3.2, the range of the azimuth angle ϕ in a practical detectable region becomes $-\frac{\pi}{2} + \phi_{\min} \leq \phi \leq \frac{\pi}{2} - \phi_{\min}$. Since $\Delta\phi = \pi/K$ is chosen to be very small (for sufficient accuracy of (3.8)), we can simply approximate $\phi_{\min}$: $\phi_{\min} = S\Delta\phi$, where $S = \left[\frac{\phi_{\min}}{\Delta\phi}\right]$. Here, "[ ]" denotes the rounding operator. With such an approximation, the range of the azimuth angle ϕ in the practical detectable region (for both cases of absence and presence of shadowing)

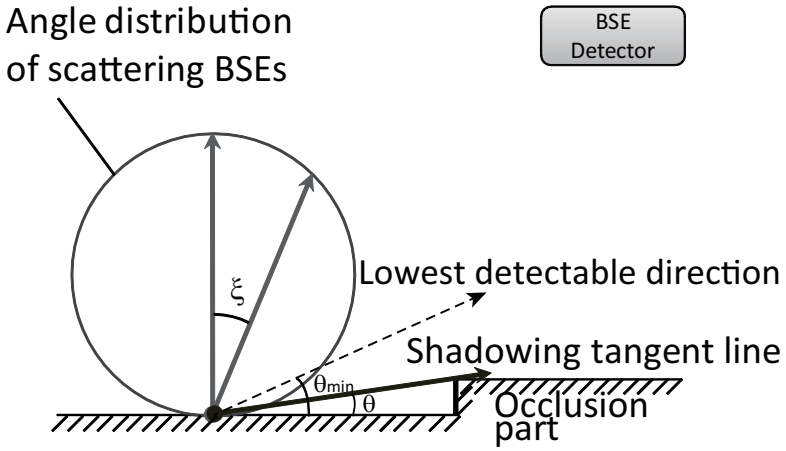

Figure 3.3: Geometric representations of practical factors $\theta_{\min}$.

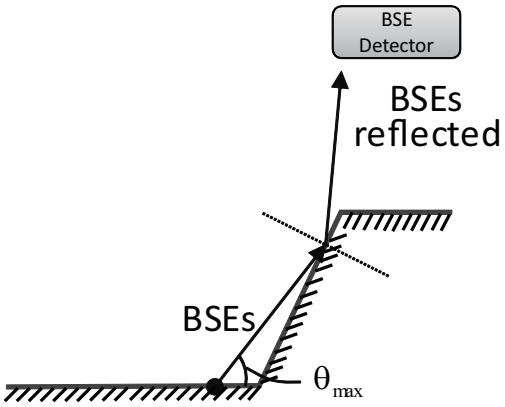

Figure 3.4: Geometric representations of practical factors $\theta_{\max}$.

is $\phi_S \leq \phi \leq \phi_{K-S}$.

The Parameter $\theta_{\min}$

On account of the finite size of practical detectors, electrons with an emission direction near the horizontal plane may not be collected. We therefore introduce another parameter $\theta_{\min}$ to model the lowest detectable direction. In the case of absence of shadowing, the range of ξ can only be up to the lowest detectable direction. In the some cases of presence of shadowing, such as the case in Fig. 3.3, when the shadowing tangent line is below the lowest detectable direction, i.e., $\frac{\pi}{2} - \theta(\phi) > \frac{\pi}{2} - \theta_{\min}$, there is in fact no shadowing in the ϕ direction and the range of ξ is only up to the lowest detectable direction as well.

The Parameter $\theta_{\max}$

We previously gave the ideal assumption on occlusion phenomena, that the BSEs below the shadowing tangent line were totally absorbed. However, as illustrated in Fig. 3.4, when the emission direction of the BSEs is nearly parallel to the slope of the shadowing object (considerably large incident angle), the electrons are likely to be re-scattered rather than absorbed into the shadowing objects. Such reflected portion of BSEs is consequently detectable, which gives rise to increasing the corresponding image intensity and decreasing shadowing effects. While this phenomenon is generally difficult to model exactly due to the complicated dependence on the structure of the occlusion part, we thus approximately model it in a simple yet practically useful way by setting another threshold, $\theta_{\max}$, for the shadowing angle. When the shadowing angle is larger than $\theta_{\max}$, it is set to $\theta_{\max}$ to eliminate false shadowing effects resulted from unshadowed portion (reflected portion) of BSEs.

3.3.2 Modified SCM

Summarizing these practical factors, we can modify the detectable regions for both cases of absence and presence of shadowing, which take the following forms:

$$\Omega : \begin{cases} \phi_{S+1} \leq \phi \leq \phi_{K-S}, \\ 0 \leq \xi \leq \dfrac{\pi}{2} - \theta_{\min}, \end{cases} \tag{3.10}$$

and

$$\Omega^S = \bigcup_{i=S+1}^{K-S} \Omega_i^S, \tag{3.11}$$

where,

$$\Omega_i^S : \begin{cases} \phi_{i-1} \leq \phi \leq \phi_i, \\ 0 \leq \xi \leq \dfrac{\pi}{2} - \theta_i, \ (\theta_i = \theta_{\min} \quad \text{if } \theta_i < \theta_{\min}; \theta_{\max} \text{if } \theta_i > \theta_{\max}). \end{cases} \tag{3.12}$$

It is quite straightforward to derive new BSE intensity formulas from (3.3) and (3.8), which take the following forms:

$$\mathrm{BSE}_{\text{shadowless}} = \frac{\eta_0}{K(n+1)} \cdot (K - 2S)(1 - \sin^{n+1} \theta_{\min}), \tag{3.13}$$

$$\mathrm{BSE} = \frac{\eta_0}{K(n+1)} \cdot \sum_{i=S+1}^{K-S} 1 - \sin^{n+1} \theta_i. \tag{3.14}$$

Combing the image intensity of both cases of absence (3.13) and presence (3.14) of shadowing, we ultimately obtain a modified shadowing compensation model that can be expressed as follows:

$$\mathrm{BSE}_{\text{shadowless}} = \frac{1}{R_{\text{SCM}}} \cdot \mathrm{BSE}, \tag{3.15}$$

where the detection ratio

$$R_{\mathrm{SCM}} = \frac{\sum_{i=S+1}^{K-S} 1 - \sin^{\mathrm{n}+1}\theta_i}{(K-2S)(1-\sin^{\mathrm{n}+1}\theta_{\min})}, \tag{3.16}$$

with the thresholding operation

$$\theta_i = \begin{cases} \theta_{\min} & \theta_i \leq \theta_{\min}, \\ \theta_{\max} & \theta_i \geq \theta_{\max}, \\ \theta_i & \text{otherwise}, \end{cases}$$

for $S+1 \leq i \leq K-S$.

The detection ratio R (where may utilize R to refer to R_{SCM} for convenience that can be distinguished from the context.) describes the mechanism of generation of shadowing via shadowing angles which imply occlusion amount. In fact, shadowing angles are determined by the 3D shape. Therefore the each shadowing angle should be the function of the 3D shape, i.e., $\theta_i = \theta_i(Z)$. The range of detection ratio is $R \in (0, 1]$, where $R = 1$ indicates absence of shadowing with all shadowing angles being zero. It is less likely that the detection ratio is zero, which implies the surrounding height is infinity. It is different from the shadowing in optic photometric stereo [36, 17, 37, 38, 39], in which shadowing means a point is unobservable from some camera and the intensity is ideally zero.

One advantage of the shadowing compensation model is that it is no need for us to treat the regions with shadowing errors separately from those without such errors, because the shadowless case is special case of shadowing with detection ration $R = 1$ (shadowing angles should be zero after implementation of the thresholding operator). Therefore, in contrast to a literature example [11], this case does not require an image segmentation process to extract shadowing regions, which is substantially difficult to implement automatically.

In comparison with the primitive model (3.9), the modified one should be more accurate and flexible. Applying model (3.15) to a measured BSE image (BL or BR) at each point (pixel), we could estimate the underlying corresponding shadowless BSE image intensities from the measured ones, provided the shadowing angles for each point are known.

3.4 Concluding Remarks

In this chapter, we have introduced a shadowing compensation model though modeling the image intensities in both cases of absence and presence of shadowing. The main difference of the both cases lies in the detectable region. For convenience of modeling, we model the detectable regions in two steps. In the first step, the modeling is done under the ideal setting. In the second step, we take the practical factors into consideration and modify the shadowing compensation model.

SCM have modeled the shadowing generation process and related the underlying shadowless image intensity to the corresponding observed one though shadowing angles. It is thus make it possible to infer underlying shadowing images and consequently eliminate shadowing errors in both images and reconstructions, once shadowing angles can be obtained. This, in fact, will turn out to be the key idea for de-shadowing in the following chapter.

Chapter 4. Variational Reconstruction with De-shadowing

In this chapter, we present our robust SEM photometric stereo. The reconstruction and de-shadowing (eliminate shadowing errors) together are formulated as a constrained optimization problem via a variational approach, which is equivalent to maximum-a-posteriori problem in the point of view of statistics. We adopt an iterative scheme to solve the optimization problem, which performs commutatively between the compensation of image intensities and the modification of the corresponding 3D shape, can effectively provide both an accurate 3D shape and compensated shadowless images after convergence.

4.1 Conceptualization

With a true 3D shape, we can calculate the shadowing angles and derive the underlying shadowless images from the original measured shadowed images using SCM. On the other hand, if shadowless images are provided, gradient measurements derived via Suganuma's equation could be accurate enough to estimate a reliable 3D shape. However, both these situations are the targets we are striving toward, and the problem essentially boils down to something such as a "chicken-and-egg" dilemma.

We formulate reconstruction and de-shadowing as a constraint optimization problem. As shown in Fig. 4.1, we propose an iterative solution to the problem, that operates commutatively between shadowing compensation of the BSE images using the shadowing compensation model and reconstruction of the 3D shape from the compensated BSE images based on Suganuma's equation for calculating the gradient and a proposed noise-robust regularization optimization method for estimating shape from the gradient. After convergence of the iterative process, both a reliable 3D shape and shadowless images are provided.

4.2 Variational formulation

With the gradient measurement model (2.1) and shadowing compensation model (3.15), we formulate the reconstruction problem as following: minimize

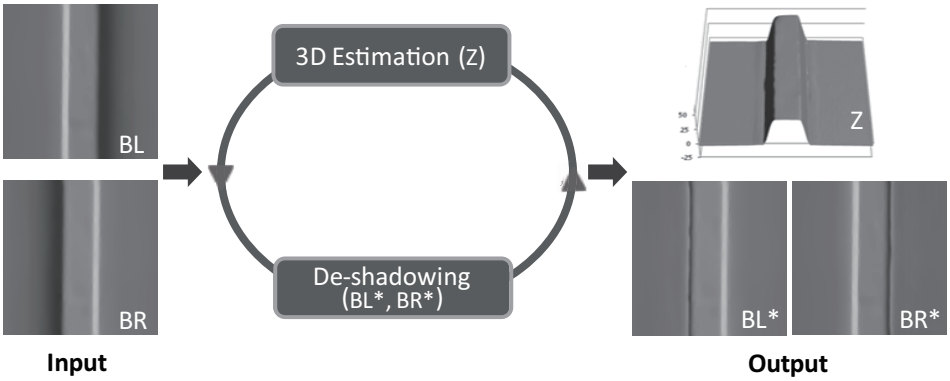

Figure 4.1: Framework of our proposed SEM photometric stereo. Given observed images (BL and BR), the method iteratively eliminates shadowing errors in images and modifies 3D shape. The algorithm will finally output the reconstructed 3D shape (Z) and underlying shadowless images (BL* and BR*).

$$\mathbf{E} = \iint_{\mathcal{D}} \left[\left(\frac{\partial Z}{\partial x} - k \frac{\mathrm{BL}^{*2} - \mathrm{BR}^{*2}}{(\mathrm{BL_n} + \mathrm{BR_n})^2} \right)^2 + \lambda \left| \nabla Z \right| \right] dxdy, \tag{4.1}$$

$$s.t. \quad \begin{cases} \mathrm{BL}^* = \dfrac{\mathrm{BL}}{R_L}, \\ \mathrm{BR}^* = \dfrac{\mathrm{BR}}{R_R}, \end{cases} \tag{4.2}$$

over some domain of interest $\mathcal{D}$ in the plane, where BL* and BR* are underlying shadowless left and right images, R_L and R_R denote corresponding detection ratio, λ is a parameter and $|\nabla Z| = \sqrt{(\frac{\partial Z}{\partial x})^2 + (\frac{\partial Z}{\partial y})^2}$.

The first term in (4.1), named fidelity term, is to guarantee the gradient of reconstructed shape should be consistent with the gradient measurement. For eliminating shadowing effects in reconstruction, gradient should be evaluated from shadowless images (BL* and BR*). As constraints, shadowless images are related to the corresponding observed ones (BL and BR) through our shadowing compensation model. The second term is total variation (TV) regularizer to penalize the roughness of the solution and consequently make our method be robust to noise influence in the data term. TV model can preserve edges well while removing noise effects, which has proven an effective prior for a range of problems in image processing and computer vision, such as reconstruction, motion estimation, denoising, and deblurring [25, 43, 44, 45, 46, 47, 48]. λ is a positive scalar factor that weights the relative contributions of these two terms. Note that λ depends upon the noise level of the gradient measurements; the noisier the measurements, the larger the value of λ should be. This can be obvious by the statistical interpretation as follows.

4.3 Statistical Interpretation

We may formulate (4.1) into maximum a-posteriori (MAP) problem[1]

$$Z = \arg\max \mathcal{P}(Z|p), \tag{4.3}$$

where p is the short-hand notation of the gradient measurement, i.e.,

$$p(x,y) = k\frac{\mathrm{BL}^{*2} - \mathrm{BR}^{*2}}{(\mathrm{BL_n} + \mathrm{BR_n})^2}$$

. Bayesian formula indicates that

$$\mathcal{P}(Z|p) \propto \mathcal{P}(p|Z)\mathcal{P}(Z), \tag{4.4}$$

where $\mathcal{P}(p|Z)$ and $\mathcal{P}(Z)$ denote the likelihood and prior, respectively, as follows.

$$\begin{aligned} \mathcal{P}(p|Z) &\propto \prod_{(x,y)\in\mathcal{D}} \exp\left(-\frac{\left|\frac{\partial Z}{\partial x} - p(x,y)\right|^2}{2\sigma^2}\right) \\ \mathcal{P}(Z) &\propto \prod_{(x,y)\in\mathcal{D}} \exp\left(-\frac{|\nabla Z|}{b}\right) \end{aligned} \tag{4.5}$$

where b is the variance of the Laplacian prior on ∇Z and σ^2 is the variance of the noise assumed on the gradient measurement $p(x,y)$. Taking the negative log likelihood to posteriori in (4.4) leads to

$$-\log \mathcal{P}(Z|p) = \iint_{\mathcal{D}} \frac{\left|\frac{\partial Z}{\partial x} - p(x,y)\right|^2}{2\sigma^2} dxdy + \iint_{\mathcal{D}} \frac{|\nabla Z|}{b} dxdy + \text{constant}. \tag{4.6}$$

We can thus observe that MAP (4.3) lead to exact optimization problem (4.1), with $\lambda = 2\sigma^2/b$, and the fidelity term and TV regularizer are corresponding to likelihood and prior, respectively. Suppose the Laplacian variance b is fixed, the more noisy of the data (σ^2 is large), the larger of the value should be.

4.4 Numerical Implementation

4.4.1 Iterative Reconstruction and De-shadowing

Solving such constrained optimization problem is not trivial. As mentioned in the previous section, shadowing angles arising in detection ratio (3.16) is the function of 3D shape Z, i.e. $\theta_i = \theta_i(Z)$. Therefore, substituting (4.2) into (4.1) results in $\mathbf{E}$ as a functional of Z. However, the dependence of shadowing angles on Z is very complicated. It is hopeless to have $\theta_i(Z)$ in an analytic form. Therefore, it is hard to minimize it directly. We adopt the alternating minimization scheme which performs commutatively between the following two steps:

[1] A systematic derivation of probability distributions on infinite-dimensional spaces requires a more formal derivation (introduction of measures etc). This may be beyond the scope of this paper.

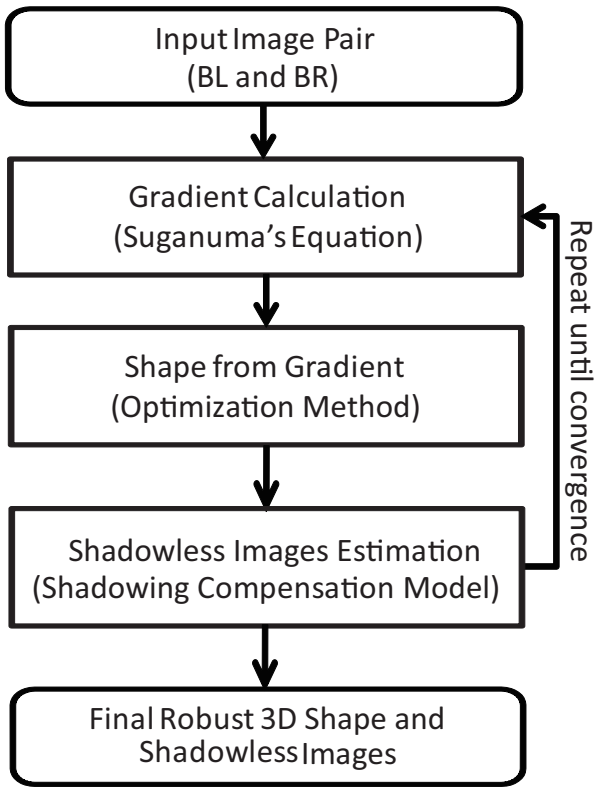

Figure 4.2: Iterative scheme for our proposed SEM photometric stereo.

1) **3D Shape reconstruction**
   Fixing BL^* and BR^* in (4.1), we can recover Z through solving the resulting unconstrained optimization problem (refer also as shape from gradient).

2) **Shadowing Compensation**
   Given Z, shadowing angles can be obtained. BL^* and BR^* can be updated with (3.16).

The algorithm (refer also to Fig. 4.2) of iterative reconstruction and de-shadowing is summarized as follows,

S1. Reconstruction of the 3D shape z_0 from the original images BL and BR.

S2. At the k^{th} iteration, the compensation ratios are calculated from the reconstructed shape Z_{k-1} from the previous iteration. Using extended shadowing compensation model to estimate shadowless images $\mathrm{BL}_{\mathrm{k}}^*$ and $\mathrm{BR}_{\mathrm{k}}^*$.

S3. A new approximation of the real shape Z_k is reconstructed from $\mathrm{BL}_{\mathrm{k}}^*$ and $\mathrm{BR}_{\mathrm{k}}^*$.

S4. If the difference between Z_k and Z_{k-1} is smaller than the given threshold, the algorithm will be terminated; otherwise, the iteration will be repeated.

The calculated compensation ratios in S2 are not the actual ones, but approximations, which can modified the images at some extent.

After convergence of the algorithm, both the reconstructed 3D shape and compensated shadowless images are obtained.

4.4.2 Shape from Gradient

In this section, the numerical implementation of shape reconstruction (minimizing (4.1)) is presented.

In the shape reconstruction procedure, we have assumed BL^* and BR^* is known. Therefore, the optimization problem is reformulated as the following functional minimization,

$$Z^* = \arg\min_Z \iint_{\mathcal{D}} \left[\left(\frac{\partial Z}{\partial x} - p(x,y) \right)^2 + \lambda \left| \nabla Z \right| \right] dxdy, \tag{4.7}$$

where

$$p(x,y) = k \frac{\mathrm{BL}^{*2} - \mathrm{BR}^{*2}}{(\mathrm{BL_n} + \mathrm{BR_n})^2}. \tag{4.8}$$

This optimization is also known as variational problem in the calculus of variations [42, 29, 50]. A fundamental result of the the calculus of variations is that the extremum of functional must satisfy the associated Euler-Lagrange equation [21]. Note that local minimum and global minimum are both examples of the extrema. It is thus that Euler-Lagrange equation is a necessary condition rather than a sufficient condition. However, the convexity of (4.7) guarantees that any local minimum must be a global minimum. Therefore, addressing (4.7) is equivalent to solve the associated Euler-Lagrange equation

$$2 \left(\frac{\partial^2 Z}{\partial x^2} - \frac{\partial p}{\partial x} \right) + \lambda \mathrm{div} \left(\frac{\nabla Z}{|\nabla Z|} \right) = 0, \tag{4.9}$$

where div is the divergence operator.

For numerical implementation, we adopt the finite difference method to discretize (4.9) according to the coordinate system $x - y$. Note that the $x - y$ coordinate system is 45° rotated from the commonly used $x' - y'$ coordinate system on account of our particular imaging setting. We regard that the $x' - y'$ coordinate system is generally more suitable for finite deference operator. Therefore we transform the Euler-Lagrange equation (4.9) into the representation in the $x' - y'$ coordinate system. As the second term $\mathrm{div}(\nabla Z/|\nabla Z|)$ is rotational invariant, it will remain the same form in the $x' - y'$ coordinate system. Therefore, substitute $\frac{\partial^2 Z}{\partial x^2}$ and $\frac{\partial p}{\partial x}$, which takes

$$\frac{\partial^2 Z}{\partial x^2} = \frac{1}{2} \left(\frac{\partial^2 Z}{\partial x'^2} + 2 \frac{\partial^2 Z}{\partial x' \partial y'} + \frac{\partial^2 Z}{\partial y'^2} \right),$$

and

$$\frac{\partial p}{\partial x} = \frac{1}{\sqrt{2}} \left(\frac{\partial p}{\partial x'} + \frac{\partial p}{\partial y'} \right),$$

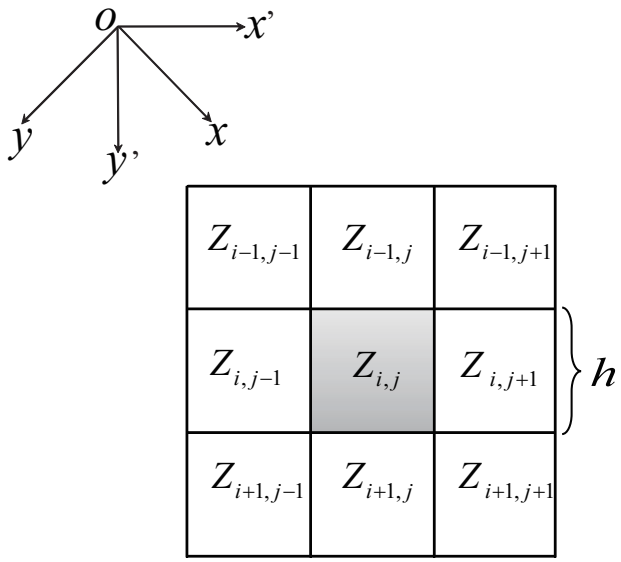

Figure 4.3: Image coordinates.

into (4.9), the Euler-Lagrange equation in the $x' - y'$ coordinate system takes the following form:

$$\left(\frac{\partial^2 Z}{\partial x'^2} + 2\frac{\partial^2 Z}{\partial x' \partial y'} + \frac{\partial^2 Z}{\partial y'^2}\right) + \lambda \text{div}\left(\frac{\nabla Z}{|\nabla Z|}\right) = \sqrt{2}\left(\frac{\partial p}{\partial x'} + \frac{\partial p}{\partial y'}\right). \tag{4.10}$$

Moreover, we adopt the commonly used Neumann boundary conditions (also known as natural boundary conditions).

Let h denote the spatial grid size. Utilizing central difference for the first term in the lefthand side and the righthand side leads to

$$\begin{aligned}
\frac{\partial^2 Z_{i,j}}{\partial x'^2} &= \frac{Z_{i,j+1} - 2Z_{i,j} + Z_{i,j-1}}{h^2} \\
\frac{\partial^2 Z_{i,j}}{\partial x' \partial y'} &= \frac{Z_{i+1,j+1} + Z_{i-1,j-1} - Z_{i+1,j-1} + Z_{i-1,j+1}}{4h^2} \\
\frac{\partial^2 Z_{i,j}}{\partial y'^2} &= \frac{Z_{i+1,j} - 2Z_{i,j} + Z_{i-1,j}}{h^2} \\
\frac{\partial p_{i,j}}{\partial x'} &= \frac{p_{i,j+1} - p_{i,j-1}}{2h} \\
\frac{\partial p_{i,j}}{\partial y'} &= \frac{p_{i+1,j} - p_{i-1,j}}{2h}
\end{aligned} \tag{4.11}$$

The discretization of the second term in the lefthand side is a bit more elaboration. In order to have a high accuracy, we take

$$\begin{aligned}
\text{div}\left(\frac{\nabla Z_{i,j}}{|\nabla Z_{i,j}|}\right) = \frac{1}{h^2}\big[&g_{i+\frac{1}{2},j} \cdot (Z_{i+1,j} - Z_{i,j}) - g_{i-\frac{1}{2},j} \cdot (Z_{i,j} - Z_{i-1,j}) \\
&+ g_{i,j+\frac{1}{2}} \cdot (Z_{i,j+1} - Z_{i,j}) - g_{i,j-\frac{1}{2}} \cdot (Z_{i,j} - Z_{i,j-1})\big],
\end{aligned} \tag{4.12}$$

where the function

$$g(|\nabla Z|) = \frac{1}{|\nabla Z|} \approx \frac{1}{\sqrt{\left(\frac{\partial Z}{\partial x'}\right)^2 + \left(\frac{\partial Z}{\partial y'}\right)^2 + \epsilon^2}}. \tag{4.13}$$

Here the small positive parameter ϵ is for stabilization. One can imagine that in the case of piecewise constant result, g can be unbounded. In our experiments, we set $\epsilon = 0.0001$. In the discretization scheme, $g_{i+\frac{1}{2},j}$, $g_{i-\frac{1}{2},j}$, $g_{i,j+\frac{1}{2}}$ and $g_{i,j-\frac{1}{2}}$ can be evaluated with the following discretization scheme.

$$\begin{aligned}
|\nabla Z_{i+\frac{1}{2},j}| &= \sqrt{\left(\frac{Z_{i+1,j}-Z_{i,j}}{h}\right)^2 + \left(\frac{Z_{i,j+1}-Z_{i,j-1}+Z_{i+1,j+1}-Z_{i+1,j-1}}{4h}\right)^2} \\
|\nabla Z_{i-\frac{1}{2},j}| &= \sqrt{\left(\frac{Z_{i,j}-Z_{i-1,j}}{h}\right)^2 + \left(\frac{Z_{i-1,j+1}-Z_{i-1,j-1}+Z_{i,j+1}-Z_{i,j-1}}{4h}\right)^2} \\
|\nabla Z_{i,j+\frac{1}{2}}| &= \sqrt{\left(\frac{Z_{i,j+1}-Z_{i,j}}{h}\right)^2 + \left(\frac{Z_{i+1,j}-Z_{i-1,j}+Z_{i+1,j+1}-Z_{i-1,j+1}}{4h}\right)^2} \\
|\nabla Z_{i,j-\frac{1}{2}}| &= \sqrt{\left(\frac{Z_{i,j}-Z_{i,j-1}}{h}\right)^2 + \left(\frac{Z_{i+1,j-1}-Z_{i-1,j-1}+Z_{i+1,j}-Z_{i-1,j}}{4h}\right)^2}
\end{aligned} \tag{4.14}$$

The finite difference operators result in a large nonlinear system. The nonlinearity is on account of g. Let $\mathbf{Z}$ denote the vector obtained from discretization of $Z(x, y)$. Treat g ($g_{i+\frac{1}{2},j}$, $g_{i-\frac{1}{2},j}$, $g_{i,j+\frac{1}{2}}$ and $g_{i,j-\frac{1}{2}}$) as coefficient, the nonlinear system can take the following Quasi-linear matrix from:

$$A(\mathbf{Z})\mathbf{Z} = \mathbf{b}, \tag{4.15}$$

where $A(\mathbf{Z})$ is large but sparse.

We adopt a so-called fixed point method [24, 51]to solve the Quasi-linear system (4.15). The key idea is to address the nonlinear problem by solving a sequence of linear systems with the nonlinear part arising in $A(\mathbf{Z})$ being fixed. The method is summarized as follows:

1) Initialize $\mathbf{Z}$ with a guess $\mathbf{Z^{(0)}}$.

2) At m^{th} iteration, fix $A(\mathbf{Z})$ with $A(\mathbf{Z^{(m-1)}})$.

3) Obtain $\mathbf{Z^{(m)}}$ by solving resulting linear system

$$A(\mathbf{Z^{(m-1)}})\mathbf{Z^{(m)}} = \mathbf{b},$$

which can be solved effectively through such as Jacobi method, Gauss-Seidel method, Successive over-relaxation, etc [49].

4) Iterate between 2) and 3) until convergence.

Note that the linear system need not be solved exactly in each iteration to yield fast convergence [24, 51].

4.5 Experimental Results

In this section, we present the results of experiments on real image data and examine the robustness and effectiveness of the proposed method under shadowing conditions.

4.5.1 Details of System Setting

The SEM used in our experiment has a general electron optics system except that the two BSE detectors are located 45° from the $x'-$axis (Fig. 4.3). Three different patterns with strong shadowing effects are used for evaluating the proposed reconstruction method, which include a standard particle with a "sphere" pattern, a semiconductor device with a "line" pattern, and a semiconductor device with a "concave" pattern having an embedded defect. The parameters used in the experiments are shown in Table 4.1. From a computational perspective, the calibration of parameters should be theoretically designed based on the information of corresponding physical processes, such as electron scattering characteristics, detectable ranges of detectors, signal conversion characteristics (conversion from the amount of detected BSEs to image intensity), etc. However, it is difficult to accurately know such information in practice. We therefore manually determine the parameters by observing that the reconstructed shape do not have distortions. As the experiments of the three patterns share the one set of parameters, we consider that it should not be overfitting for each individual case. However, in the field of SEM photometric stereo method, one set of universally utilized parameters might not be sufficient owing to the use of different materials, imaging conditions, and so on. Therefore, we recognize this as a problem for future investigation requiring some data-wise optimization of the parameters.

Table 4.1: Experimental parameters.

k	1.98
n	1.30
$\phi_{\min}$	16.9°
$\theta_{\min}$	17.5°
$\theta_{\max}$	55.0°
λ	0.15

4.5.2 Evaluation on Real Image Data

Figs. 4.4 and 4.5 show experimental results for the "sphere" pattern. In this case, the sphere particle plays the role of the occlusion. As described in the previous section, the existence of a shadowing effect results in an image intensity that is smaller than the

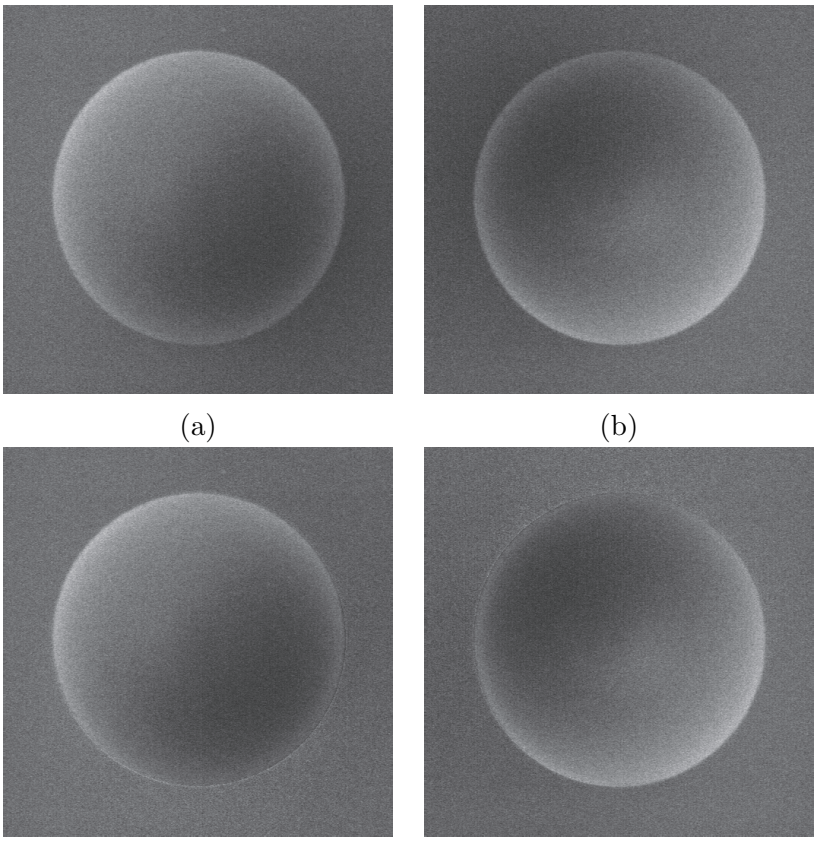

Figure 4.4: Comparison between the original and compensated images of the "sphere" pattern: (a) original BL image, (b) original BR image, (c) compensated BL image, and (d) compensated BR image.

underlying shadowless one. As mentioned before, the detectors are set along the diagonal direction with respect to the image plane. Therefore, the shadowing effects of the sphere pattern occur mainly in the area of the diagonal, (i.e., the lower-right flat region in the left image and the upper-left flat region in the right image). As shown in Fig. 4.4 (a) and (b), the brightness in the shadowing regions is less intense than that in the flat regions without shadowing. Whereas, as shown in Fig. 4.4 (c) and (d), the brightness of the flat region around the spherical particle in both the left and right compensated image demonstrates a certain uniformity, which in turn implies good compensation of the image intensities. As shown in Fig. 4.5, shape distortion in the flat region resulting from shadowing errors, i.e., a rising-slope toward the sphere, can be effectively reduced by compensation.

Figs. 4.6 and 4.7 show reconstruction results for the "line" pattern. The original left and right images (BL and BR) are shown in Fig. 4.6 (a) and (b). It is obvious that the right side of the left image and the left side of the right image are notably dark, which is, in fact, due to shadowing effects. In this case, the "line" plays the

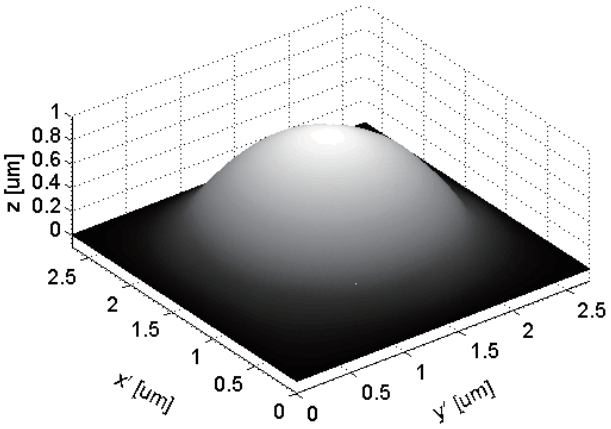

(a)

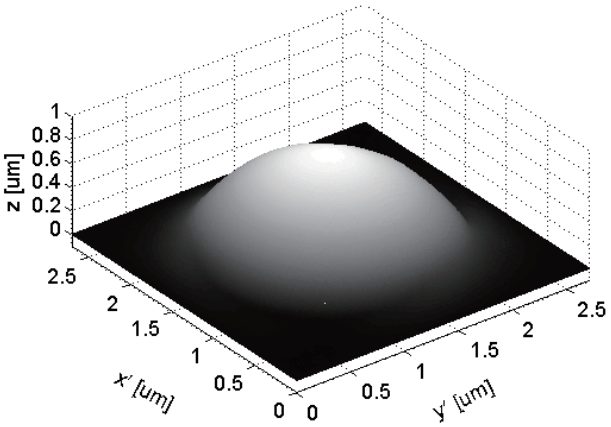

(b)

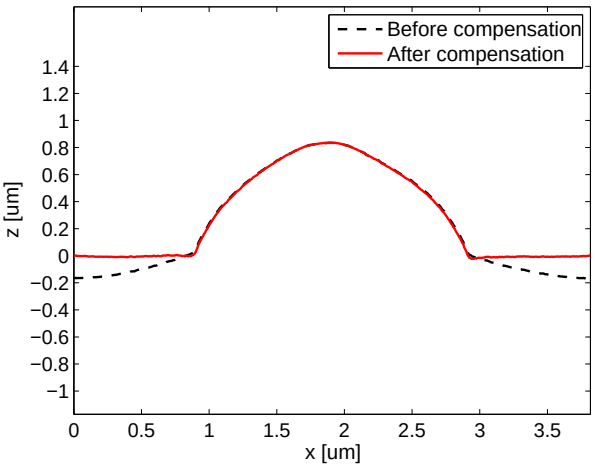

(c)

Figure 4.5: 3D surface and section profiles of "sphere" pattern before and after shadowing compensation. (a) 3D surface before compensation, (b) 3D surface after compensation, (c) diagonal section profiles.

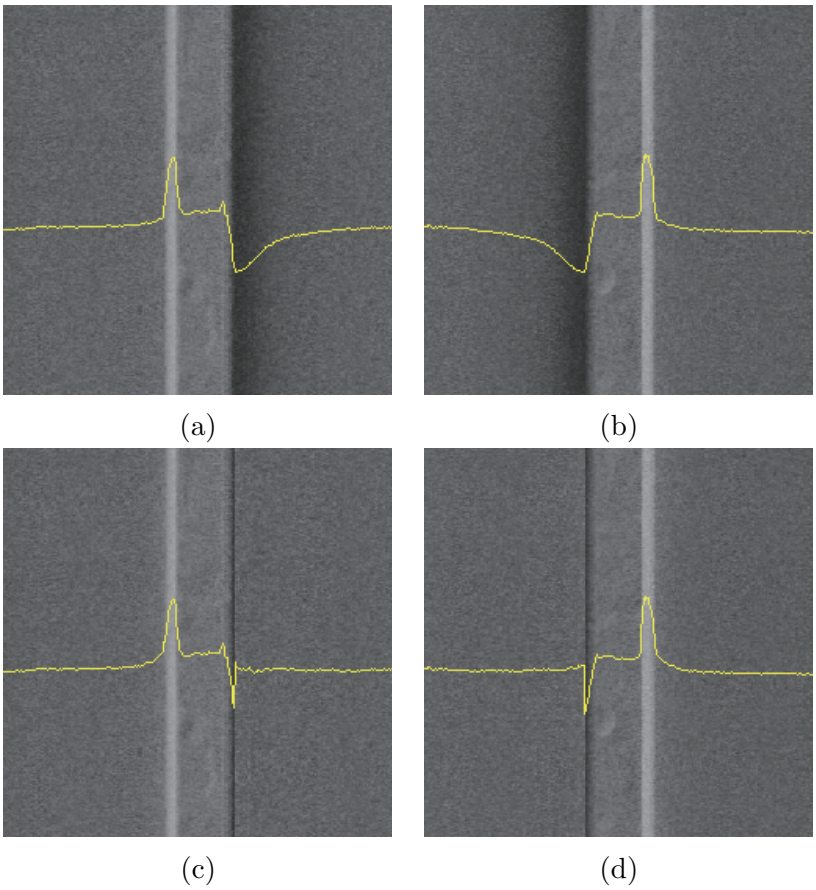

Figure 4.6: Comparison between the original and compensated images of the "line" pattern: (a) original BL image, (b) original BR image, (c) compensated BL image, and (d) compensated BR image. The plot of every image shows average column intensities.

role of the occluding object. Such shadowing errors in image intensities give rise to significant departures of the gradient measurements from true ones (zeros at ideally flat regions), which is consequently reflected in the reconstructed 3D surface as a rising slope toward the "line" (see Fig. 4.7). As shown in Fig. 4.6 (c) and (d), these dark shadowing regions in the original left and right images are effectively eliminated in the compensated images. The corresponding average intensity plots (the average is used to avoid submersion of the plot into noise) also highlight suitably compensated shadowing errors. Moreover, the reconstructed 3D surface shape and section profile also show large modifications (Fig. 4.7) in that the rising slope regions on both sides of the "line" are properly corrected to a nearly flat level.

Figs. 4.9 and 4.10 show experimental results for the "concave" pattern with an embedded defect. The topography of the pattern is much more complicated than that of the previous two cases. As observed in the original left and right images in Fig. 4.9 (a) and (b), the image brightness near the sloping region is much lower, which is obviously due to the corresponding shadowing effect. This feature is also demonstrated

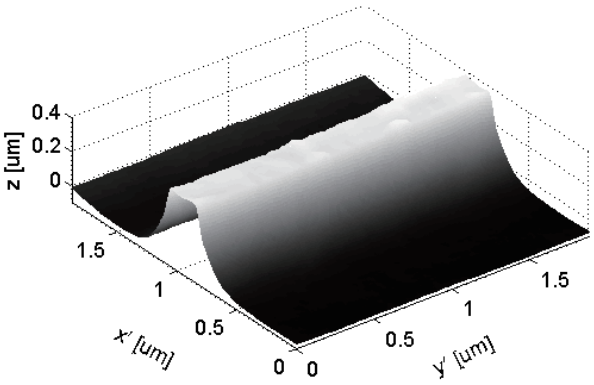

(a)

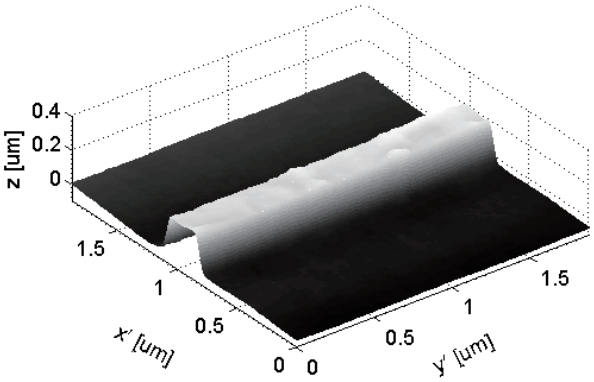

(b)

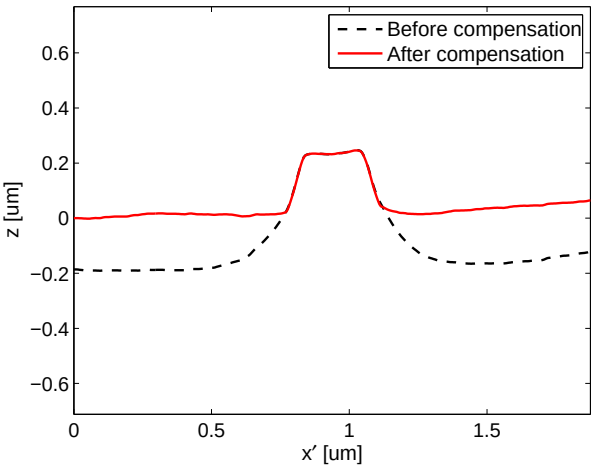

(c)

Figure 4.7: 3D surface and section profiles of "line" pattern before and after shadowing compensation. (a) 3D surface before compensation, (b) 3D surface after compensation, (c) center horizontal section profiles.

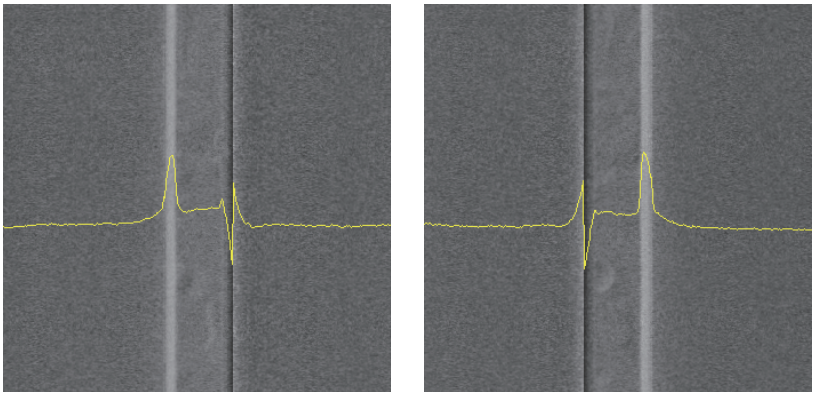

(a) (b)

Figure 4.8: Over-compensated images of the "line" pattern: (a) over-compensated BL image and (b) over-compensated BR image.

more clearly by the average intensity plots (near positions (2) and (3) in Fig. 4.10 (c)). The shadowing effect on both sides of the defect "peak" is also strong, and although it is not readily distinguishable by the image brightness, it can be clearly observed in the 3D shape. The compensated shadowless images are shown in Fig. 4.9 (c) and (d). As seen in the figure, the regions that were dark in the original left and right images now show an appropriate level of brightness. The modification is highlighted by the corresponding average intensity plots, although they are not perfectly flat. Fig. 4.10 (a) and (b) show the reconstructed 3D shape before and after shadowing compensation, respectively. As the "concave" pattern is substantially complicated to give a vivid view of the 3D surface modification afforded by the shadowing compensation process, we selected three representative section profiles, whose positions are marked in Fig. 4.10 (c). The first one is a vertical section crossing the "peak" shown in Fig. 4.10 (d). Because the "peak" is high, the shadowing effect on both sides is strong, which has a certain similarity to the "line" pattern where the "peak" plays the role of the "bar". Such shadowing errors result in a rising slope effect, as shown by the dashed line profile (before compensation), and this effect is reduced by shadowing compensation, as shown by the solid line. The other two section profiles, shown in Fig. 4.10 (e) and (f), have a similar shadowing effect. The shadowing error in the "concave" region results in a falling slope effect, leading to a deeper cavity, as shown by the dashed lines. After the shadowing compensation process, such falling slope effects are eliminated to a certain degree, as shown by the solid lines. The result implies the possibility that the shadowing compensation model is applicable to not only horizontal surfaces but mildly inclined surfaces, although our model is derived from the horizontal case.

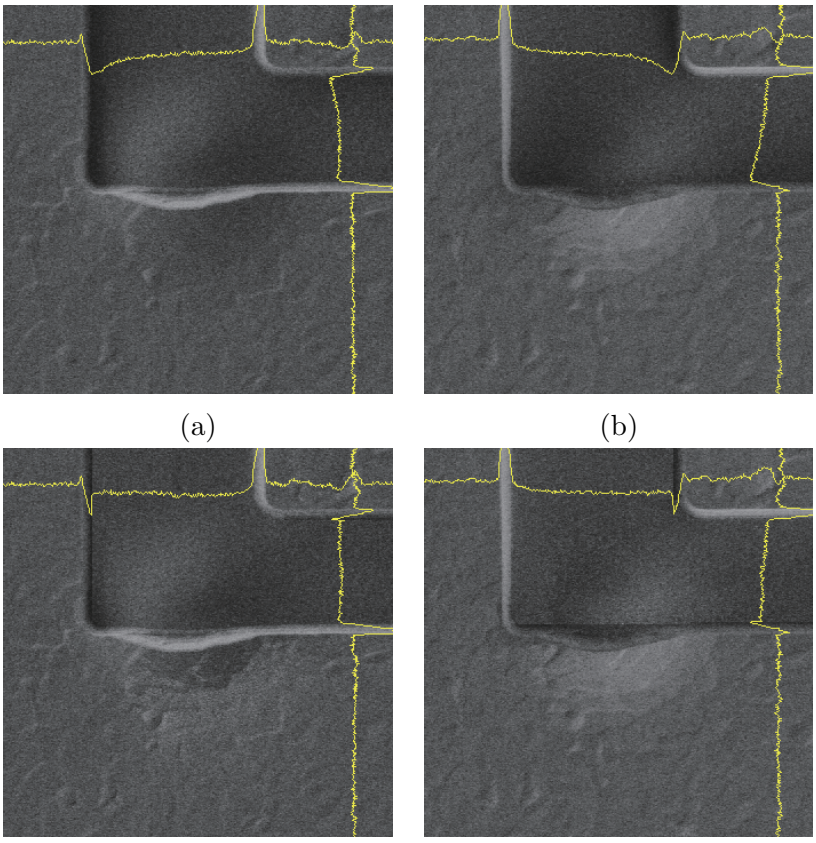

Figure 4.9: Comparison between the original and compensated images of the "concave" pattern: (a) original BL image, (b) original BR image, (c) compensated BL image, and (d) compensated BR image.

4.5.3 Analysis of $\theta_{\max}$

On account of the good illustrative property of the "line" pattern (the average intensity plot was easily drawn to demonstrate the shadowing and compensation conditions), we designed an additional experiment using the "line" pattern to demonstrate the significance of the parameter $\theta_{\max}$, which is introduced for improving the accuracy and flexibility of the shadowing compensation model (Section 3.3.1). To this end, the same computational process is implemented except that the value of $\theta_{\max}$ was set to $\frac{\pi}{2}$, which is equivalent to omitting the thresholding operation with $\theta_{\max}$. The resulting compensated shadowless image pair is shown in Fig. 4.8. Compared to the result in Fig. 4.6 (c) and (d), the average intensity plots show that shadowing regions very near to the "bar" are overcompensated resulting in much higher intensities, which indicates that the underlying true shadowing angels in that region should be smaller. The thresholding operation with $\theta_{\max}$ could generally overcome this problem well and consequently contribute greater accuracy to the shadowing compensation model.

Table 4.2: Quantitative comparison (mean absolute error in horizontal regions).

	Before compensation	After compensation
Sphere	$0.0862\mu m$	$0.0307\mu m$
Line	$0.0412\mu m$	$0.0229\mu m$

4.5.4 Quantitative Analysis

In older to quantitatively assess the de-shadowing performance of our method, we choose the "sphere" and "line" patterns on account of their good illustrative property. As the shadowing effects only exist on the background areas, the reconstruction of the sphere part and line part (no shadowing) is not affected. We thus only need to focus on the background parts. The background regions can be effectively segmented out manually from left and right images. Based on the assumption that the background parts are even, the true height can be set to zero. In order to eliminate translation of the reconstructed height Z (the shape of $Z + c$ should be identical to that of Z, where c is a constant), the reconstructed surfaces are registrated at the origin point, i.e., to translate the surfaces Z vertically to (0,0,0). We use the mean absolute error of measured height (list in Table 4.2) in background parts to evaluate the reconstruction performance. The proposed method shows much smaller deviation compared to the traditional method with no shadowing compensation.

4.6 Concluding Remarks

In this chapter, we have proposed a robust SEM photometric stereo method. The shadowing effect, a frequent occurrence in SEM imaging processes, can be effectively eliminated by the iterative scheme associated with the shadowing compensation model. The reconstructed 3D shape can be robustly and automatically obtained under an existing shadowing condition. Furthermore, the resulting left and right compensated images provide a potential opportunity for improving the imaging performance of SEM devices. The proposed method has also been verified by our experimental results, which show its robustness and effectiveness.

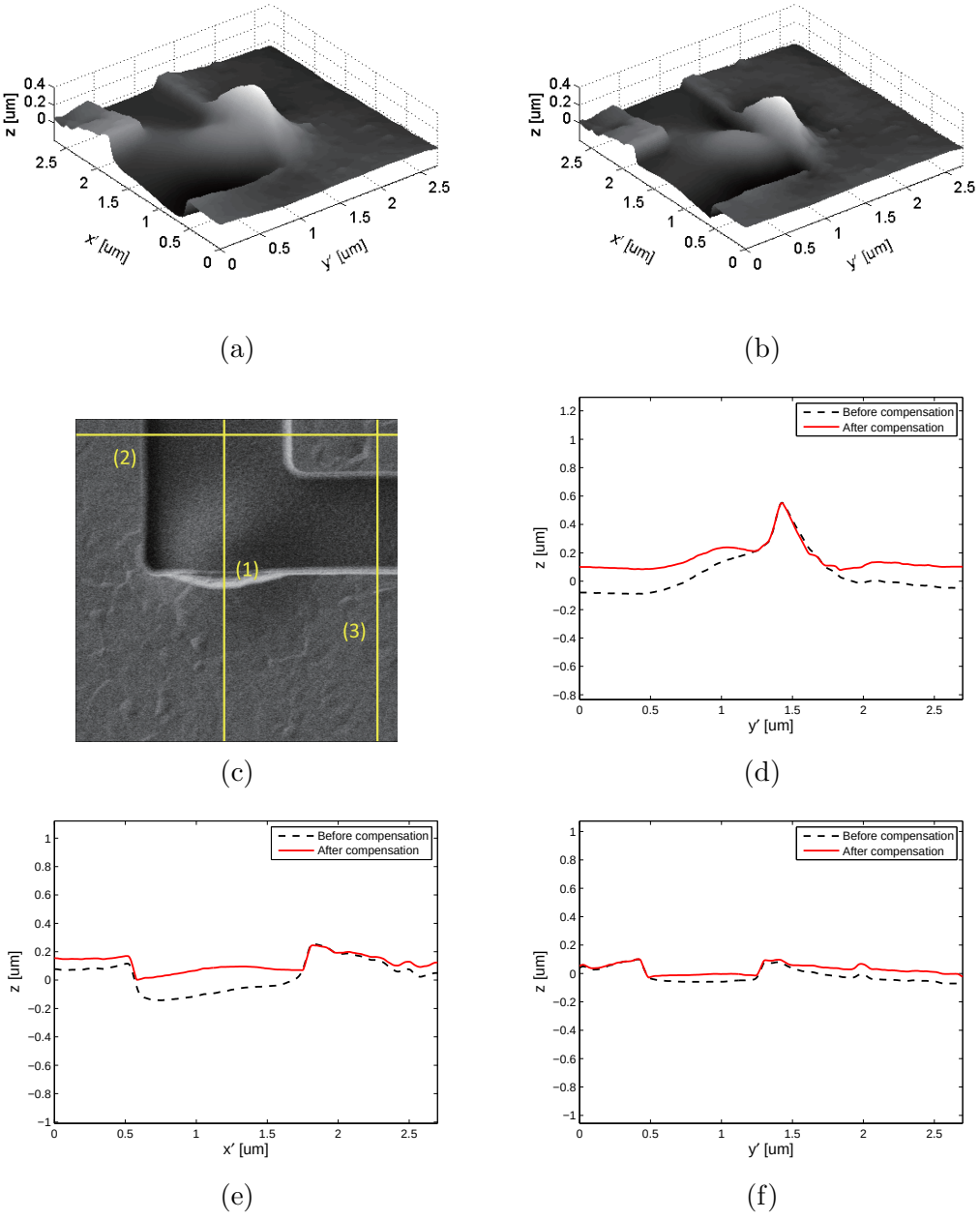

Figure 4.10: Three-dimensional surface and section profiles of the "concave" pattern before and after shadowing compensation: (a) 3D surface before compensation, (b) 3D surface after compensation, (c) selected section profile positions marked on the left image BL, (d) vertical section profiles crossing the defect at position (1), (e) horizontal section profiles at position (2), and (f) vertical section profiles at position (3).

Chapter 5. Extended Shadowing Compensation Model

This chapter presents an extension to the shadowing compensation model in order to improve the model accuracy in the shadowing regions on the general curved surfaces. The extended model removes the earlier restrictive assumption that the shadowing effects exist only on horizontal surfaces. This model is developed in an analogous way through modeling image intensities in both the absence and presence of shadowing. A numerical solution is proposed to resolve the implicit expressions for double integrals in the model.

5.1 Conceptualization

We have introduced the shadowing compensation model in Chapter 3. In the theoretical derivation of the model, we assumed that shadowing effects exist only in the horizontal region. This assumption simplifies the model and introduces certain benefits, such as compact explicit solutions, convenient calculations. However, when the model is applied to shadowing regions on surfaces with sufficiently large inclinations, the resulting errors are large.

To increase accuracy and expand the scope of the shadowing compensation model, we extend the model from horizontal surfaces to general inclined surfaces (as shown in Fig. 5.1). Analogous to the previous scenario in the horizontal case, the extended shadowing compensation model is derived by modeling the shadowing generation process, i.e., the image intensity in both the absence and presence of shadowing, while abandoning the restrictive assumption that shadowing effects exist only on horizontal surfaces. Unlike the previous model, the extended shadowing compensation model does not have a closed-form solution. Hence, we explore a numerical approach that is also computationally efficient. The two main contributions of this study are as follows: (1) We extend the shadowing compensation model from horizontal surfaces to general inclined surfaces. (2) We present numerical solutions for the extended shadowing compensation model.

5.2 Improvement

To increase the accuracy on general inclined surfaces and extend the scope of the model, we abandon the restrictive assumption and extend the model from horizontal surfaces to more general inclined surfaces. Although the modeling procedure of the

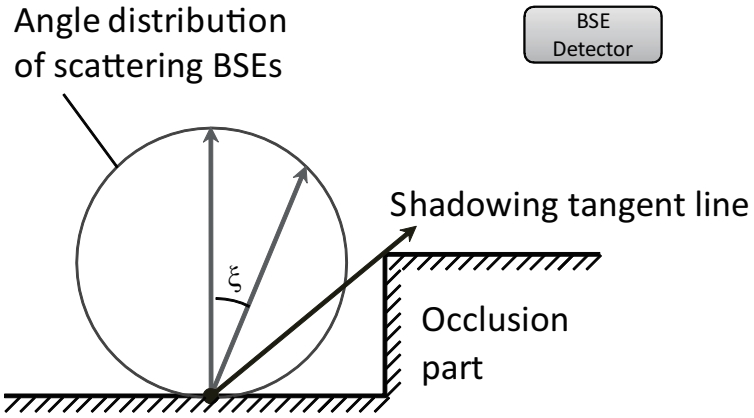

(a) Shadowing on the horizontal surface.

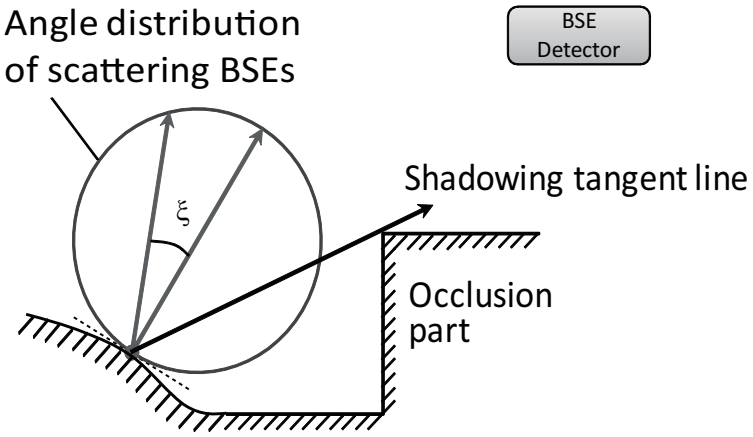

(b) Shadowing on the inclined surface.

Figure 5.1: Shadowing effects. BSEs emitted in a direction below the shadowing tangent line are generally absorbed by the occlusion region and consequently are not collected by the detector.

extended shadowing compensation model is analogous to that of the previous model, the mathematical derivation can be much more complicated.

5.2.1 Coordinate System

Figure 5.2 shows the coordinate system for 3D measurements. The Z-axis is coincident with the incident primary electron (PE) beam, the x-axis is the direction along which two detectors are positioned, and the y-axis is perpendicular to both the x and z axes according to the right-hand rule. The surface of the measuring specimen can be represented as $Z(x, y)$. The normal to the tangent plane of the surface is $\vec{m} = \left(-\frac{\partial Z}{\partial x}, -\frac{\partial Z}{\partial y}, 1\right)$. For an arbitrary emitting direction of BSEs $\vec{v} =$

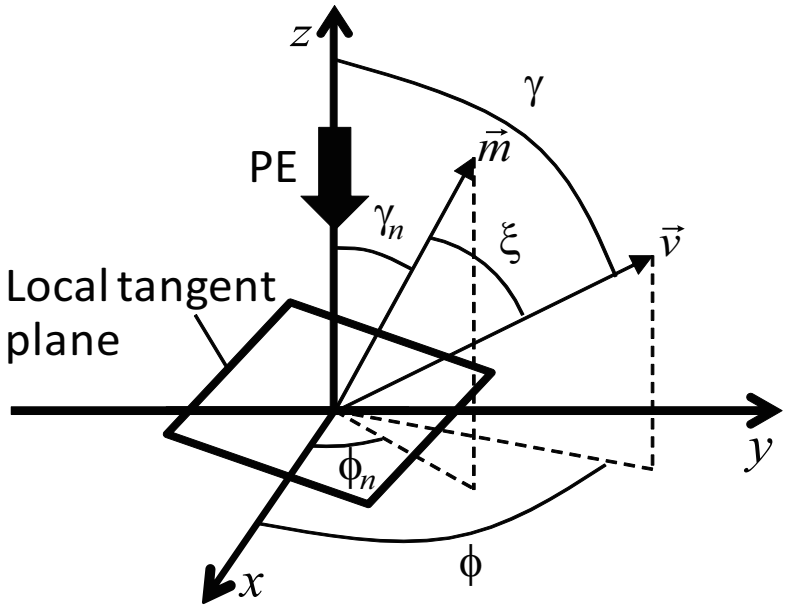

Figure 5.2: Coordinate system.

$(\cos\phi\sin\gamma, \sin\phi\sin\gamma, \cos\gamma)$, the angle distribution takes the following form:

$$\frac{d\eta}{d\omega} = \frac{\eta_0}{\pi}\left(\frac{\cos\gamma - \frac{\partial Z}{\partial x}\cos\phi\sin\gamma - \frac{\partial Z}{\partial y}\sin\phi\sin\gamma}{\sqrt{1+\left(\frac{\partial Z}{\partial x}\right)^2+\left(\frac{\partial Z}{\partial y}\right)^2}}\right)^n, \tag{5.1}$$

where γ and ϕ denote the zenith and azimuth angles, respectively.

5.2.2 BSE Intensity in the Absence of Shadowing

In the non-shadowing case, the detectable range of the azimuth angle ϕ for detectors should ideally be $-\frac{\pi}{2} \le \phi \le \frac{\pi}{2}$. Nonetheless, BSEs in the region where ϕ is near $\pm\frac{\pi}{2}$ generally cannot be detected owing to the practical limitations of the detector. Therefore, we introduce the parameter $\phi_{\min}$ to model this shortfall (same in Chapter 3); then the range of the azimuth angle in the practical detectable region should be $-\frac{\pi}{2} + \phi_{\min} \le \phi \le \frac{\pi}{2} - \phi_{\min}$.

The range of the zenith angle γ is more complicated. As shown in Fig. 5.3, different inclination conditions of the surface give rise to different expressions for the upper limit. In the case of Fig. 5.3 (a), the upper limit of the zenith angle γ is up to the surface tangent direction $\vec{t} = \left(\cos\phi, \sin\phi, \cos\phi\frac{\partial Z}{\partial x} + \sin\phi\frac{\partial Z}{\partial y}\right)$, i.e., the intersection of the tangent plane and the zenith integration plane (see also Fig. 5.4), which takes the following form:

$$\gamma_{\vec{t}}(\phi) = \arccos\left(\frac{M}{\sqrt{1+M^2}}\right), \tag{5.2}$$

where $M = \cos\phi\frac{\partial Z}{\partial x} + \sin\phi\frac{\partial Z}{\partial y}$.

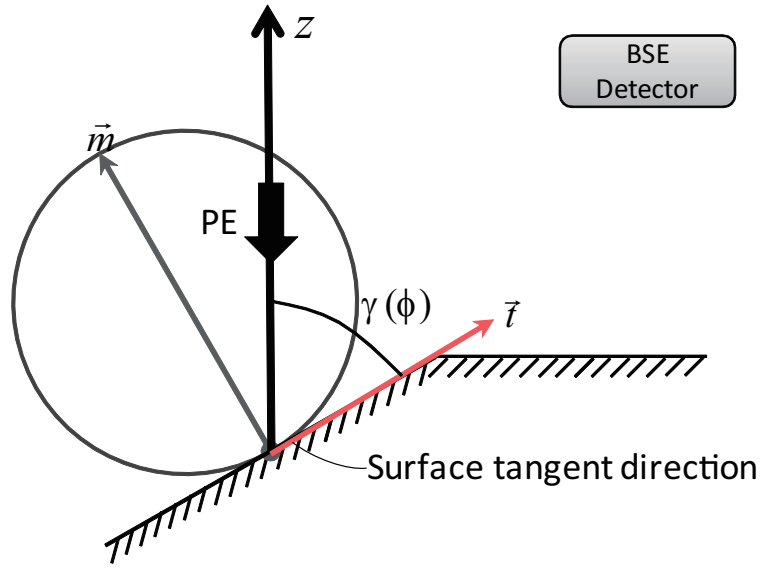

(a)

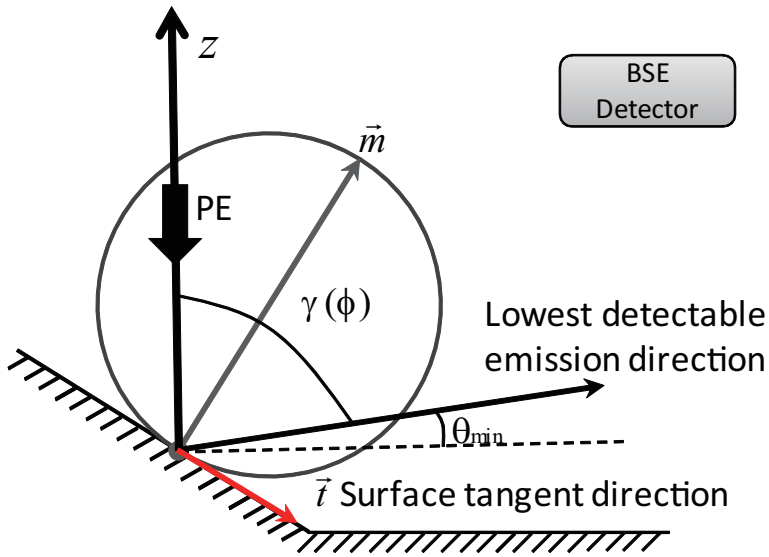

(b)

Figure 5.3: Zenith ranges in the absence of shadowing. (a) The upper limit of the zenith angle is up to the surface tangent direction. (b) The upper limit of the zenith angle can be only up to the lowest detectable emission direction, electrons below this direction generally cannot be collected by a detector.

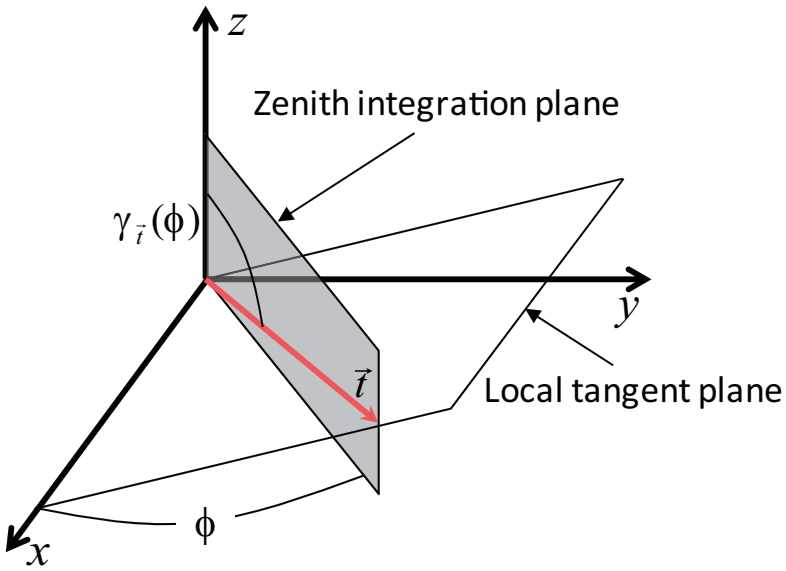

Figure 5.4: One case of upper limit of zenith angle.

In the case of Fig. 5.3 (b), the surface tangent direction is below the horizontal direction. However, the BSE detector can only ideally collect BSEs above the horizontal direction. The electrons with emission angles below the horizontal direction generally cannot be detected. Furthermore, because of the finite size of practical detectors, electrons with an emission direction near the horizontal plane may not be collected. Another parameter $\theta_{\min}$ is introduced to model such practical factors (same in Chapter 3). Therefore, in this case, the upper limit of the zenith angle cannot be up to the surface tangent direction, but only up to $\frac{\pi}{2} - \theta_{\min}$.

Summarizing the different cases, the upper limit of the zenith angle should be $\gamma(\phi) = \min\left\{\frac{\pi}{2} - \theta_{\min}, \gamma_{\vec{t}}(\phi)\right\}$, and the detectable region Ω in the case of non-shadowing can take the following form:

$$\Omega : \begin{cases} -\dfrac{\pi}{2} + \phi_{\min} \leq \phi \leq \dfrac{\pi}{2} - \phi_{\min} \\ 0 \leq \gamma \leq \min\left\{\dfrac{\pi}{2} - \theta_{\min}, \gamma_{\vec{t}}(\phi)\right\} \end{cases} \tag{5.3}$$

The image intensity (signal output) on each detector is proportional to the number of collected electrons, which can be modeled by the following double integral:

$$\mathrm{BSE}_{\mathrm{shadowless}} = \iint_{\Omega} \frac{\eta_0}{\pi} (\cos\xi)^n d\omega = \frac{\eta_0}{\pi} \iint_{\Omega} I(\phi, \gamma) d\phi d\gamma, \tag{5.4}$$

where the integrand[1]

$$I(\phi,\gamma)=\left(\frac{\cos\gamma-\frac{\partial Z}{\partial x}\cos\phi\sin\gamma-\frac{\partial Z}{\partial y}\sin\phi\sin\gamma}{\sqrt{1+\left(\frac{\partial Z}{\partial x}\right)^2+\left(\frac{\partial Z}{\partial y}\right)^2}}\right)^n\sin\gamma. \tag{5.5}$$

Unfortunately, this integral cannot be evaluated via elementary functions.

5.2.3 BSE Intensity in the Presence of Shadowing

In the shadowing case, the azimuth range of the detectable region should be identical to that of the non-shadowing case. However, the zenith range is generally smaller because of occlusion. As shown in Fig. 5.5, the portion of the BSEs from the shadowing tangent line to the local surface tangent direction is occluded and generally cannot be collected by the corresponding detector. The range of the zenith angle should be $0\le\gamma\le\gamma_{\vec{t}}(\phi)-\theta(\phi)$, where $\theta(\phi)$ is the shadowing angle defined as the angle between the shadowing tangent line and surface tangent direction. Nevertheless, it is likely that the shadowing tangent direction is below the lowest detectable emission direction, i.e., $\gamma_{\vec{t}}(\phi)-\theta(\phi)>\frac{\pi}{2}-\theta(\phi)$. So, in fact, there is no shadowing in the ϕ direction (see also Fig. 5.5 (b)). Including both cases for the zenith range, the upper limit of the zenith angle should be $\gamma(\phi)=\min\left\{\frac{\pi}{2}-\theta_{\min},\gamma_{\vec{t}}(\phi)-\theta(\phi)\right\}$. Therefore, the detectable region should take the following form:

$$\Omega^S:\begin{cases}-\dfrac{\pi}{2}+\phi_{\min}\le\phi\le\dfrac{\pi}{2}-\phi_{\min}\\ 0\le\gamma\le\min\left\{\dfrac{\pi}{2}-\theta_{\min},\gamma_{\vec{t}}(\phi)-\theta(\phi)\right\}\end{cases} \tag{5.6}$$

However, to optimize the process for modeling shadowing effects, a practical factor must be considered. As illustrated in Fig. 5.6, when the emission direction of the BSEs is nearly parallel to the slope of the shadowing object, electrons are likely to be reflected rather than absorbed. We therefore simply set a threshold, $\theta_{\max}$, for the shadowing angle. When the shadowing angle is larger than $\theta_{\max}$, it is set to $\theta_{\max}$.

Similar to the case of absence of shadowing, the observed image intensity can also be modeled by the following double integral:

$$\mathrm{BSE}=\iint_{\Omega^S}\frac{\eta_0}{\pi}(\cos\xi)^n d\omega=\frac{\eta_0}{\pi}\iint_{\Omega^S}I(\phi,\gamma)d\phi d\gamma. \tag{5.7}$$

Here the integrand $I(\phi,\gamma)$ takes the same form as (5.5). This integral cannot be evaluated via elementary functions.

[1]More rigorously, the integrand should be represented as $I(\phi,\gamma,\frac{\partial z}{\partial x},\frac{\partial z}{\partial y})$, and consequently the image intensity in the non-shadowing case would be $\mathrm{BSE}_{\mathrm{shadowless}}(\frac{\partial z}{\partial x},\frac{\partial z}{\partial y})$, which would be differing corresponding to the inclination condition of the local tangent plane.

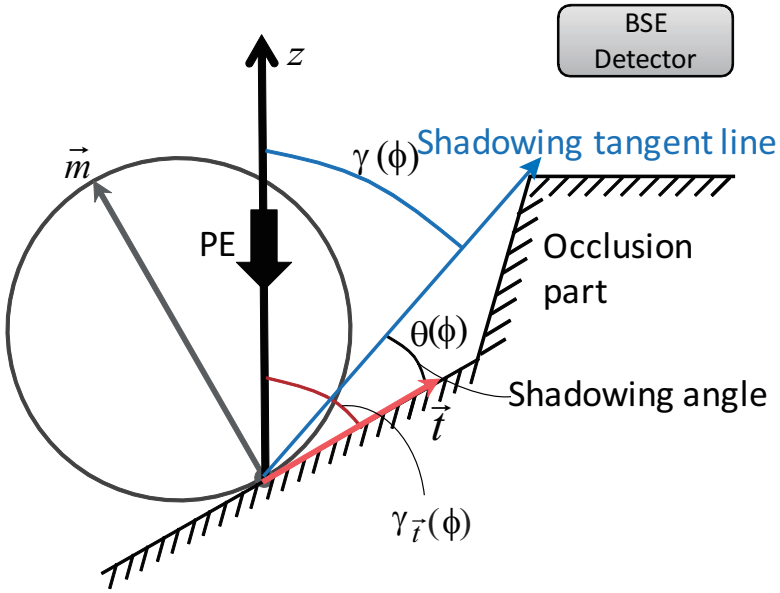

(a)

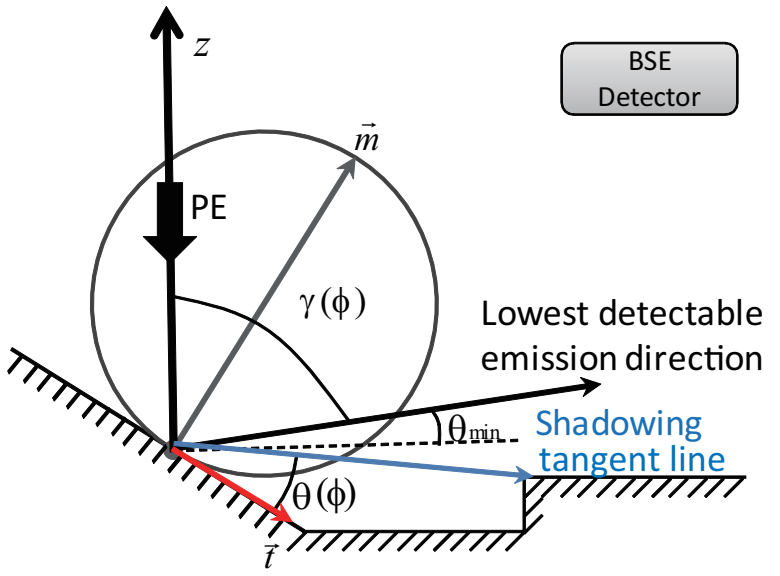

(b)

Figure 5.5: Zenith ranges in the presence of shadowing. (a) The upper limit of the zenith angle is up to the shadowing tangent line. (b) The upper limit of the zenith angle can only be up to the lowest detectable emission direction; electrons below this direction generally cannot be collected by a detector, which indicates no shadowing in fact.

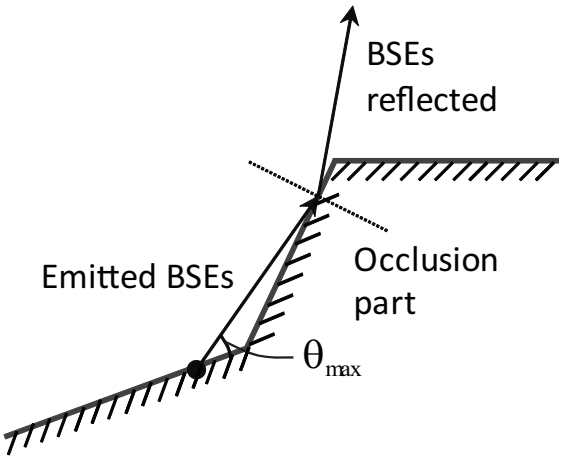

Figure 5.6: Illustration of the practical factor modeled by $\theta_{\max}$.

5.2.4 Extended Shadowing Compensation Model

Equation (5.7) models the observed image intensity that may include the presence of shadowing effects. In fact, the shadowless case can be considered to be a special shadowing case in which the shadowing angle $\theta(\phi) = 0$. Generalizing this observation, we can deduce the following extended shadowing compensation model by combining (5.4) and (5.7).

$$\mathrm{BSE}_{\mathrm{shadowless}} = \frac{1}{R_{\mathrm{ESCM}}} \cdot \mathrm{BSE}. \tag{5.8}$$

Here the detection ratio R can be expressed as

$$R_{\mathrm{ESCM}} = \frac{\iint_{\Omega^s} I(\phi,\gamma) d\phi d\gamma}{\iint_{\Omega} I(\phi,\gamma) d\phi d\gamma}. \tag{5.9}$$

Unlike the horizontal case, the compensation ratio (5.9) cannot be evaluated explicitly.

5.3 Numerical solution

Since the two integral in (5.9) cannot be evaluated explicitly, the extended shadowing compensation model cannot take an explicit form. Therefore, we must explore a numerical solution for the model.

For a uniform discretization of the domain of integration (detectable region), we can simply merge the two detectable regions Ω and Ω^s into a quarter sphere Ω_Q : $-\frac{\pi}{2} \le \phi \le \frac{\pi}{2}, 0 \le \gamma \le \frac{\pi}{2}$, as both are subsets of Ω_Q, i.e., $\Omega,\ \Omega^s \subseteq \Omega_Q$. Ω_Q can be discretized into $K \times L$ elementary regions with the azimuth step $\Delta\phi$ and the zenith step $\Delta\gamma$, see Fig. 5.7. The step sizes of $\Delta\phi$ and $\Delta\gamma$ should be set sufficiently small to ensure accuracy. The detectable region (Ω or Ω^s) can be regularized in the following way:

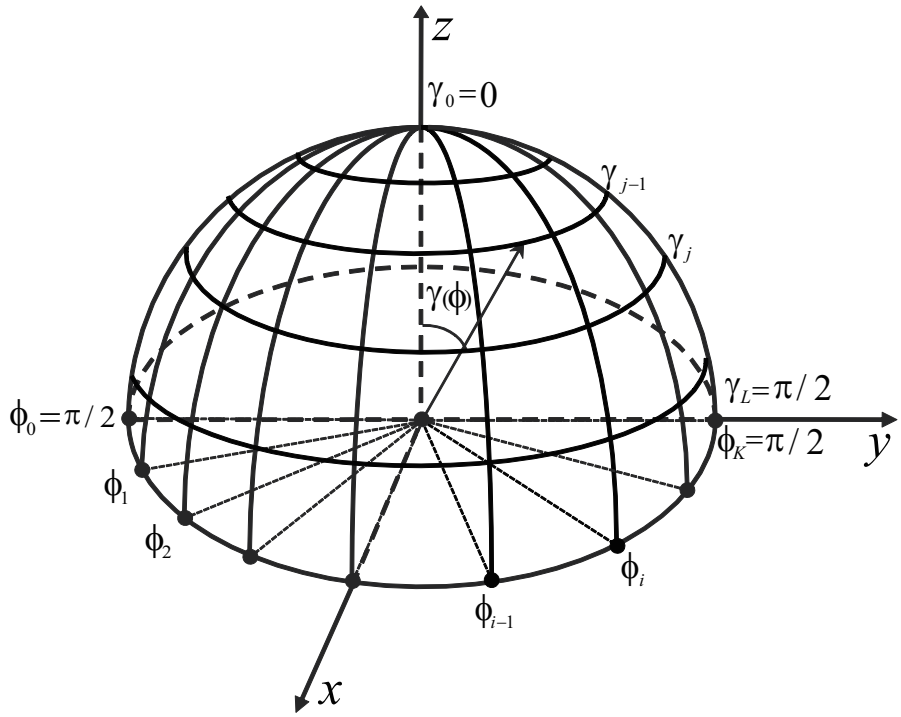

(a) Discretization shown in 3D.

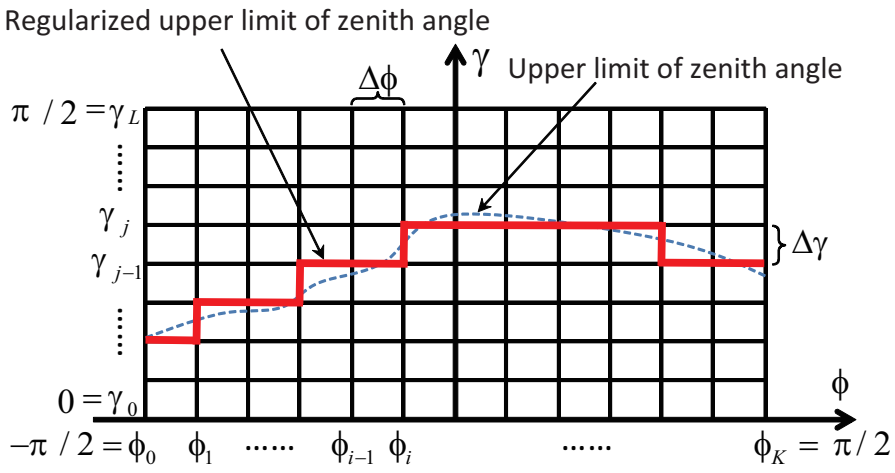

(b) Discretization shown in 2D.

Figure 5.7: Discretization of the detectable region. (a) Illustration of discretization of Ω_Q shown in 3D space. (b) Illustration of discretization of Ω_Q shown in 2D space and regularization of detectable region.

(1) $\phi_{\min} \approx S \cdot \Delta\phi$, where $S = \left[\frac{\phi_{\min}}{\Delta\phi}\right]$. The azimuth range can be approximated as $\phi_S \leq \phi \leq \phi_{K-S}$.

(2) $\gamma(\phi) \approx J_i \cdot \Delta\gamma$ for $\phi_{i-1} \leq \phi \leq \phi_i$, $S+1 \leq i \leq K-S$. Here $J_i = \left[\frac{\gamma(\phi_{i-1}+\Delta\phi/2)}{\Delta\gamma}\right]$. The zenith range can be approximated as $0 = \gamma_0 \leq \gamma \leq \gamma_{J_i}$, for $S+1 \leq i \leq K-S$, see Fig. 5.7 (b).

Therefore, the regularized detectable region (Ω or Ω^s) can be expressed as follows:

$$\Omega/\Omega^S : \begin{cases} \phi_S \leq \phi \leq \phi_{K-S} \\ \gamma_0 \leq \gamma \leq \gamma_{J_i}, \quad S+1 \leq i \leq K-S \end{cases} \tag{5.10}$$

The integrand within each elementary rectangular region ($\phi_{i-1} \leq \phi \leq \phi_i$, $\gamma_{j-1} \leq \gamma \leq \gamma_j$ for $S+1 \leq i \leq K-S$, $1 \leq j \leq J_i$) can be approximated as $I(\phi,\gamma) \approx I_{ij} = I(\phi_{i-1} + \Delta\phi/2, \gamma_{j-1} + \Delta\gamma/2)$.

With these approximations, we can ultimately achieve numerical solutions for the two double integrals:

$$\iint_{\Omega/\Omega^S} I(\phi,\gamma)d\phi d\gamma \approx \sum_{i=S+1}^{K-S}\sum_{j=1}^{J_i} I_{ij}\Delta\phi\Delta\gamma. \tag{5.11}$$

Consequently, the compensation ratio (5.9) can be numerically calculated with this numerical method.

5.4 Experimental Results

In this section, we present the results of experiments on real image data and examine the robustness and effectiveness of the proposed method under shadowing conditions. Two different patterns of semiconductor devices with strong shadowing effects existing on both flat regions and inclined regions were used for evaluating the performance of the proposed extended shadowing compensation model (ESCM) and the previous shadowing compensation model (SCM). Both devices had embedded defects, which included a "semi-line" pattern and a "concave" pattern. The SEM used in our experiment performs raster scanning along the direction located 45° from the x-axis. (The x-axis is defined as the direction along which the detectors are positioned.) Therefore, the x'-axis and the y'-axis consistent with the image array are defined for convenience in displaying results.

5.4.1 Comparison on Real Image Data

Fig. 5.8 and Fig. 5.9 show the experimental results for the "semi-line" pattern. Fig. 5.8 (a) shows the original left and right images. It is obvious that the lower part near the "semi-line" in the original left image and the upper and upper left part near the "semi-line" in the original right image are notably dark, which is, in fact, owing

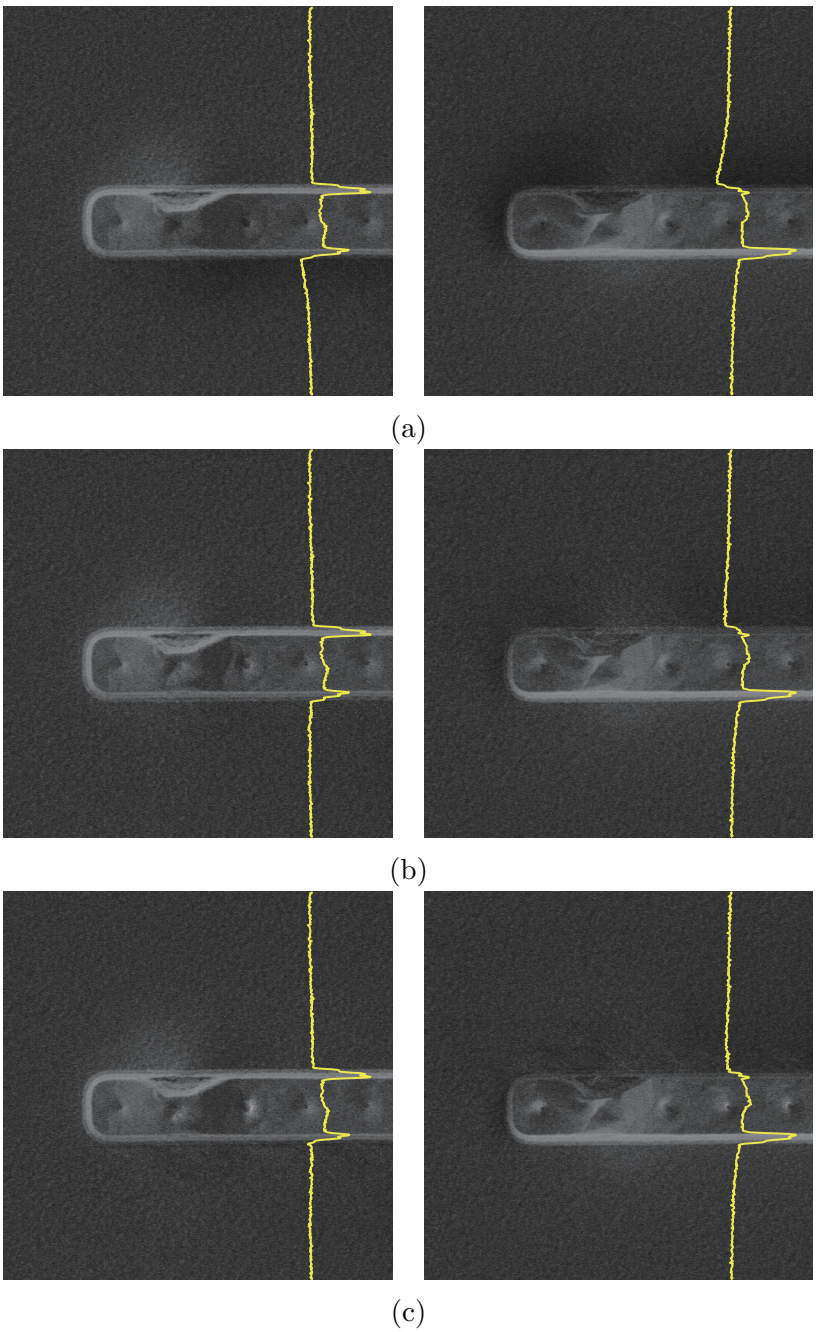

(a)

(b)

(c)

Figure 5.8: Comparison between the original and compensated images of the "semi-line" pattern: (a) original left and right images, (b) compensated left and right images via SCM, and (c) compensated left and right images via ESCM.

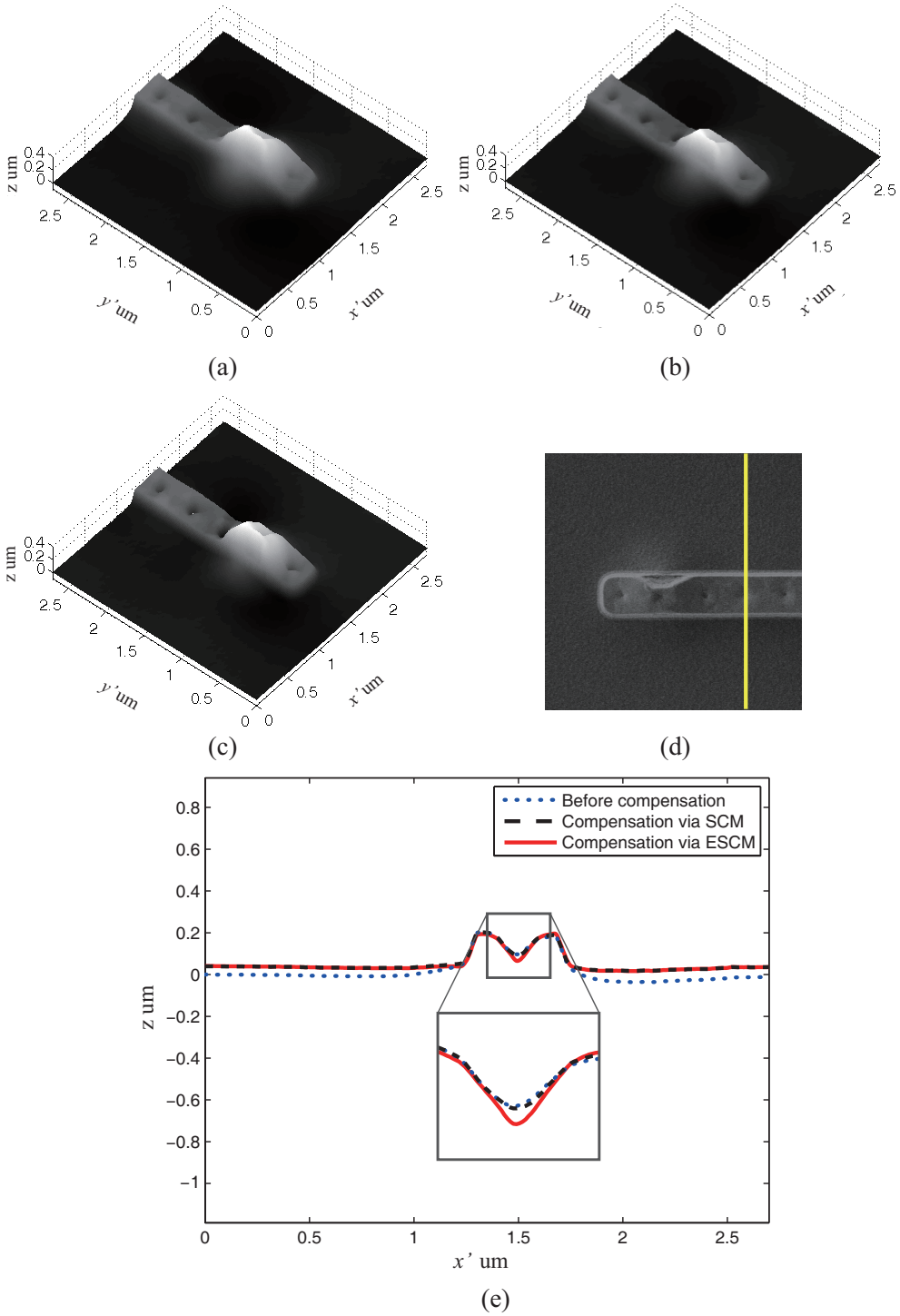

Figure 5.9: Comparison of three-dimensional surfaces and section profiles of the "semi-line" pattern: (a) 3D surface before compensation, (b) 3D surface after compensation via SCM, (c) 3D surface after compensation via ESCM, (d) selected section profile position marked on the original left image and (e) section profiles at position marked in (d).

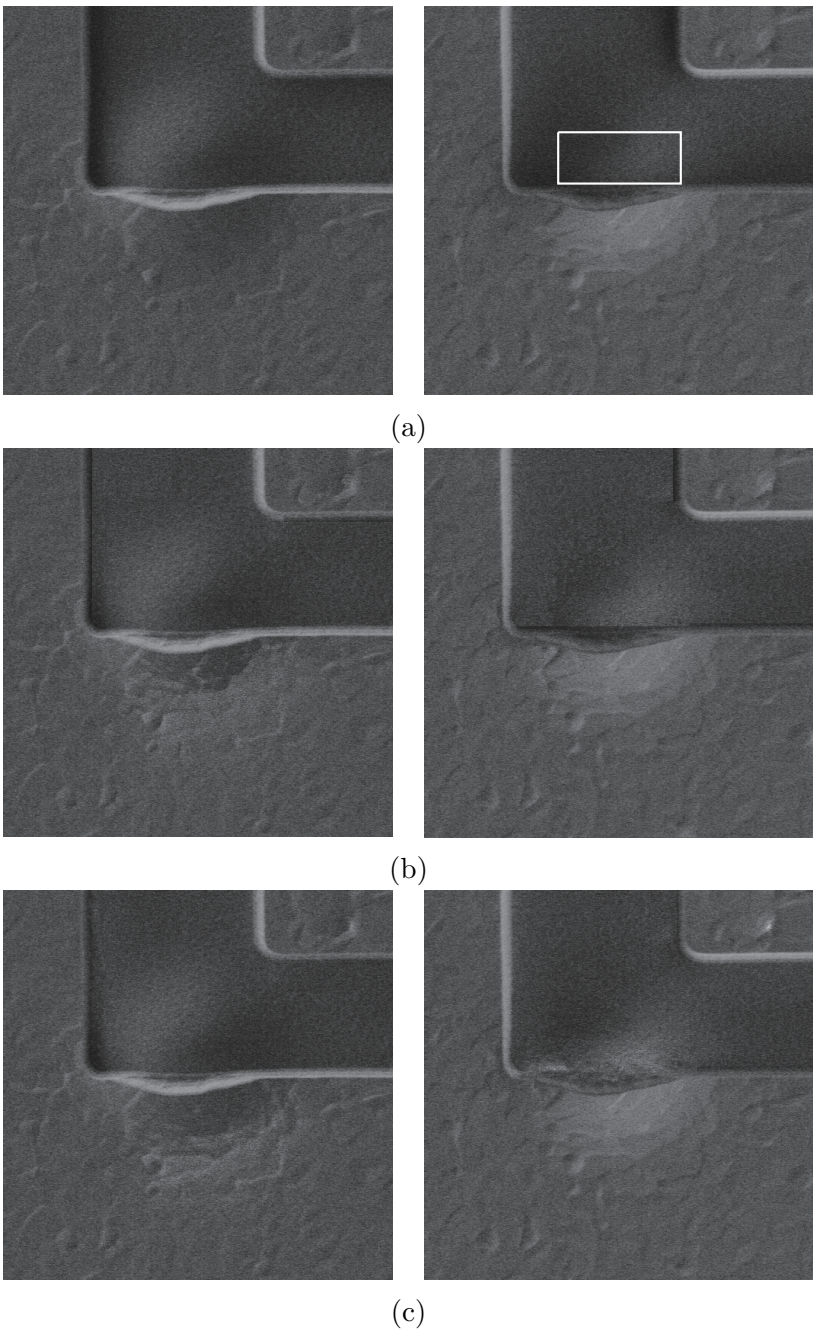

(a)

(b)

(c)

Figure 5.10: Comparison between the original and compensated images of the "concave" pattern: (a) original left (upper) and right (lower) images, marked region of interest (ROI) for quantitative analysis, (b) compensated left (upper) and right (lower) images via SCM, and (c) compensated left (upper) and right (lower) images via ESCM.

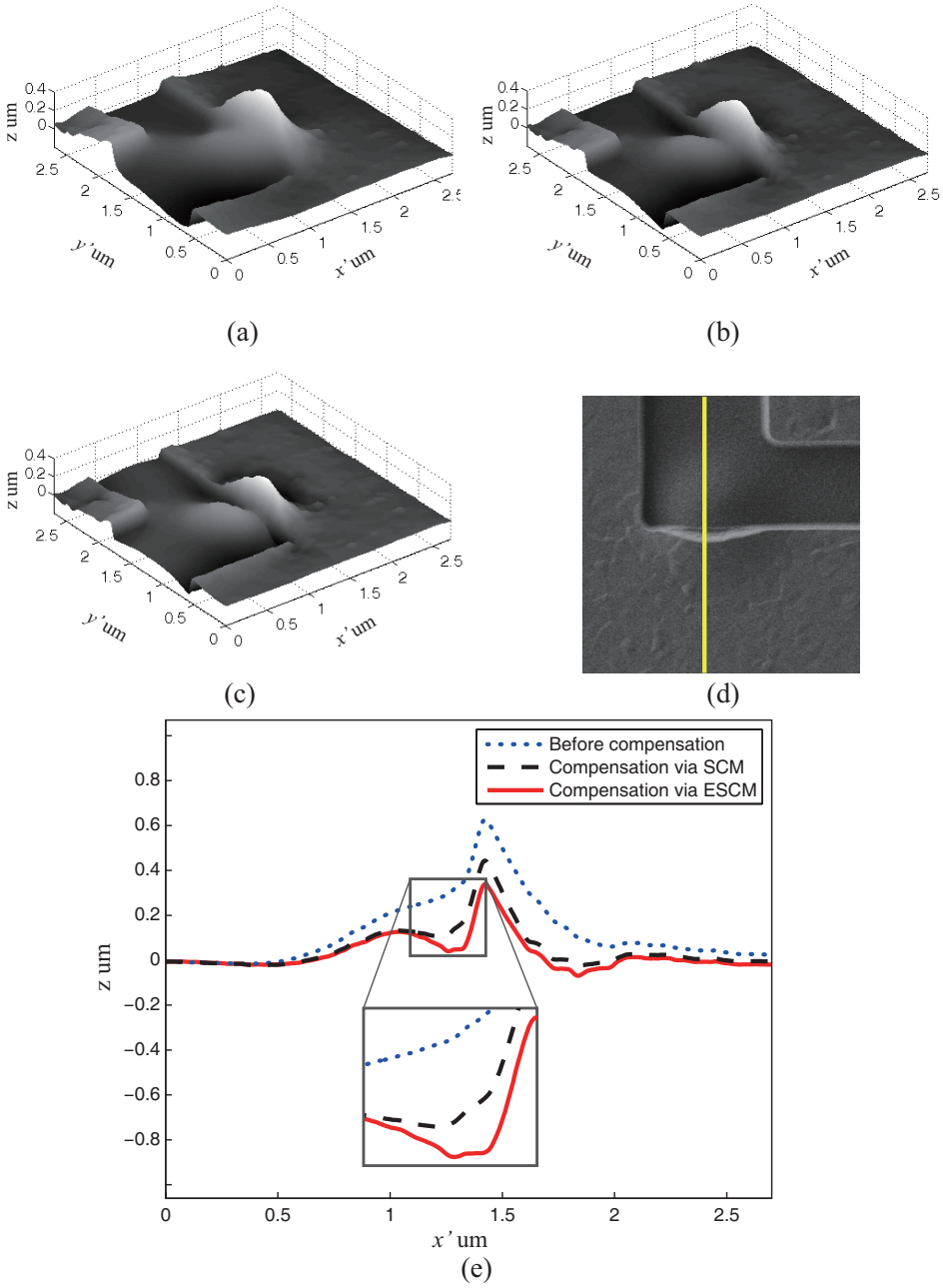

Figure 5.11: Comparison of three-dimensional surfaces and section profiles of the "concave" pattern: (a) 3D surface before compensation, (b) 3D surface after compensation via SCM, (c) 3D surface after compensation via ESCM, (d) selected section profile position marked on the original left image and (e) section profiles at position marked in (d).

to shadowing effects. Such shadowing effects can be more clearly demonstrated using average image intensity plots (the average is used to avoid submersion of the plot into noise). In this case, the "semi-line" part plays the role of an occlusion part. Such shadowing errors in image intensities give rise to significant departures of the gradient measurements from the true ones (zeros at ideally flat regions); this is reflected in the reconstructed 3D surface as a "rising slope" toward the "semi-line" part (see the 3D surface in Fig. 5.9 (a) and section profiles in Fig. 5.9 (e)). Besides shadowing effects in the horizontal area around the "semi-line" part, strong shadowing effects are also present in the dimple regions inside the "semi-line" part, where the surface is not horizontal but inclined.

Fig. 5.8 (b) and Fig. 5.9 (b) show the compensated images and the 3D surface of the "semi-line" pattern via SCM, and Fig. 5.8 (c) and Fig. 5.9 (c) show the compensated images and 3D surface of the "semi-line" pattern via ESCM, respectively. Both ESCM and SCM achieve proper performance of shadowing compensation in the horizontal shadowing region around the 'semi-line" part. In the compensated left and right images, the brightness of the flat regions around the "semi-line" part demonstrates a certain uniformity with that in the other flat regions without shadowing effects. The corresponding average intensity plots also highlight suitabe compensation of the shadowing errors in the flat regions. Moreover, the reconstructed 3D surface shape and section profiles also show large modifications (see Fig. 5.9 (b), (c), and (e)) in the "rising slope" regions on both sides of the "semi-line, "where the shape is properly corrected to a nearly flat level, as it should be.

However, ESCM can perform even better in the shadowing region of inclined surfaces, as shown in the dimple regions. As shown in Fig. 5.9 (e) (since the dimple part is too small to give a vivid view, the figure in that part is magnified), the compensated section profile within the dimple part via SCM shows little modification, which nearly coincides with the profile before compensation. But the compensation profile of ESCM reveals large modifications, indicating that ESCM may perform better on surfaces having large inclinations.

Fig. 5.10 and Fig. 5.11 show experimental results for the "concave" pattern. The embedded defect caused a very high "peak" part in the semiconductor device. Therefore, the shadowing effects on both sides of the defect "peak" are quite strong. Since the "peak" part is very high and plays the significant role of an occluding part, it causes a "rising slope" effect, that is analogous to the previous "semi-line" case. Note that the shadowing regions are not horizontal, but have large inclinations. Although the inclinations are not readily distinguishable by the image brightness, they can be clearly observed in the 3D shape and the corresponding section profile.

Fig. 5.10 (b) and Fig. 5.11 (b) show the compensated images and 3D surface of the "concave" pattern via SCM, and Fig. 5.10 (c) and Fig. 5.11 (c) show the compensated images and 3D surface of the "concave" pattern via ESCM. As vividly demonstrated in Fig. 5.11 (e), the compensated shape of the defect part (shadowing effect on the

inclined surface) via ESCM reveals better modification than that via SCM, although SCM also shows large modifications. The defect part in the compensated 3D shape in Fig. 5.11 (c) becomes more distinguishable and recognizable. The experimental results in turn indicate that compared with SEM, ESCM can generally achieve comparative performance in horizontal regions and even better performance on inclined surfaces.

5.4.2 Convergence Analysis

In the experiments, we use the difference of reconstructed surface between two successive iterations to reflect the convergence property of the iterative shadowing compensation algorithm, given by $e^k = \frac{1}{MN}\sqrt{\sum_{i=1}^{M}\sum_{j=1}^{N}\left(\frac{z^k(i,j) - z^{k-1}(i,j)}{h}\right)^2}$. Here k represents iterative step index, i and j refer to image row and column indices, M and N denote image height and width, and h is pixel size to make the metric e^k dimensionless. Fig. 5.12 (a) and (b) show the convergence processes of semi-line pattern and concave pattern, respectively, where the iteration number is set to 20. As observed in both cases, the method can converge quickly. In practice, we will set a threshold value T, say $T = 10^{-3}$, to terminate the algorithm earlier if $e^k < T$ at some step k.

A high speed implementation of our method has not yet been examined. The average computing time per each step with image size 512×512 is, currently, about 67.3 seconds in C++ on a 2.93GHz PC with 4G memory. However, we realize that it should be as a future work to improve the computational efficiency by means of exploring efficient numerical methods (such as multigrid method [31, 40, 41, 52, 53]) or parallel computing (GPU implementation, for instance).

5.4.3 Quantitative Analysis

For a quantitative assessment of our method, the most straightforward way should be comparing reconstruction results to the corresponding actual ones. However, it is generally difficult to obtained the height of defect parts. Because of lack of ground truth data, we alternatively adopt a somewhat indirect evaluation method. We manually select a region of interest (ROI) in the right image of the "concave" pattern marked in Fig. 5.10 (a), where the region contains strong shadow on the curved surface. Ideally, the image intensity in the ROI should have a one-to-one mapping to the corresponding gradient value of the surface if the intensity is ideally correct (without noise or shadowing errors). Because, from the physical imaging point of view, each point with a distinct inclination (gradient) on the surface gives rise to the corresponding unique and distinct intensity value. However, as shown in Fig. 5.13 (a) (Here we scale the gradient value by ignoring the constant parts in Suganuma's equation (2.1) for convenience.), such uniqueness will not hold when the intensity is polluted by random signal noise or shadowing errors. Our idea is that the data should be more compact to be closer to the one-to-one mapping

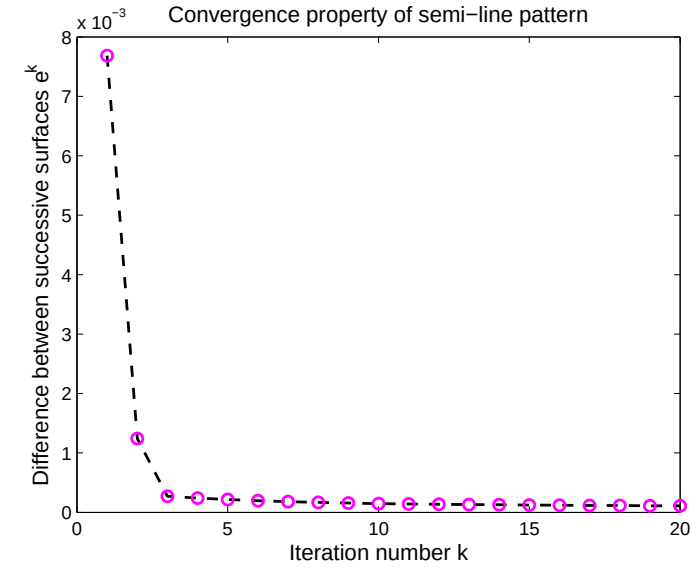

(a)

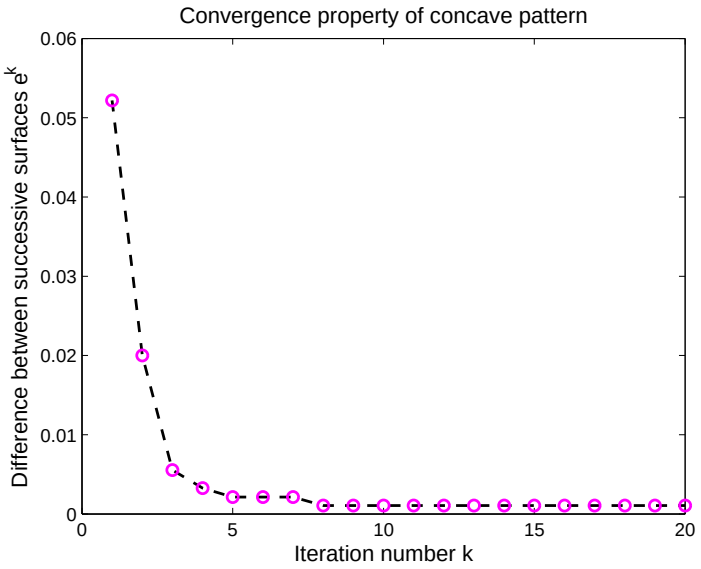

(b)

Figure 5.12: Convergence processes of the iterative shadowing compensation algorithm. (a) "Semi-line" pattern. (b) "Concave" pattern.

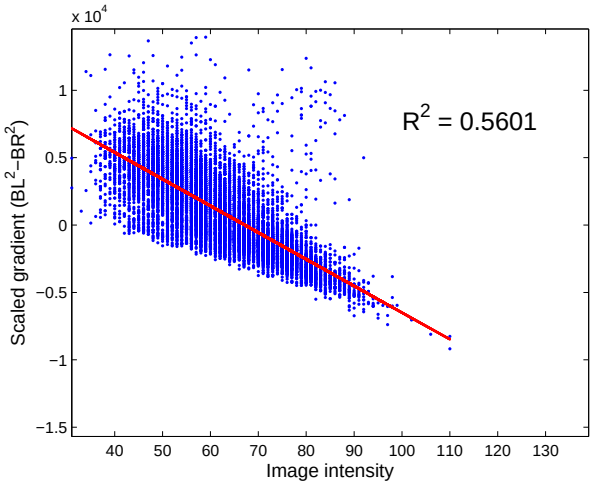

(a)

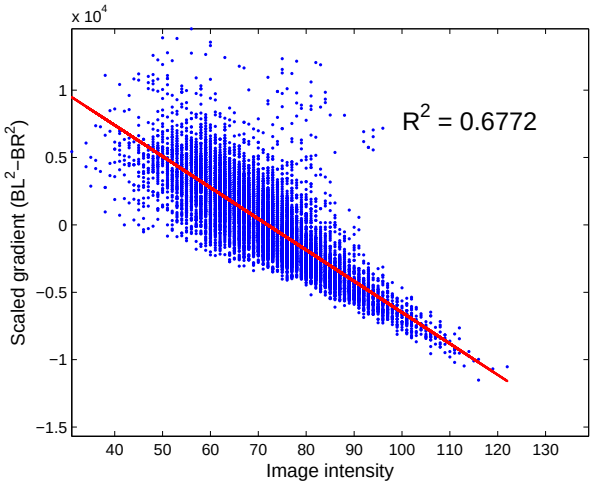

(b)

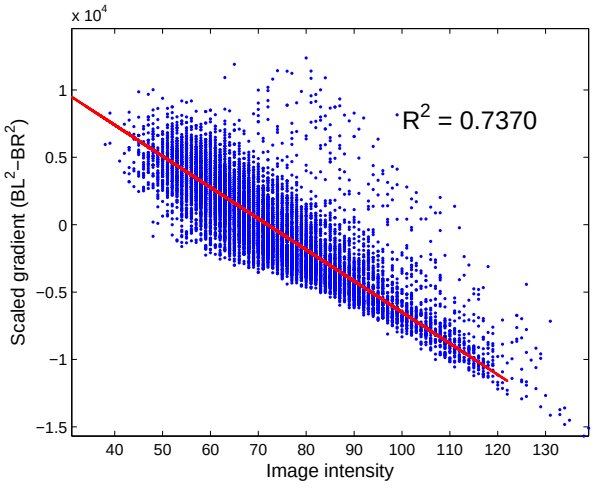

(c)

Figure 5.13: Quantitative evaluation of shadowing compensation by compactness between image intensity and gradient within the ROI marked in Fig. 5.10 (a): (a) before compensation, (b) compensation via SCM, and (c) compensation via ESCM.

if the shadowing errors are properly eliminated or reduced. The difficulty is that the mapping is related to the shape of the surface and thus unknown. We ultimate employ the linear model based on the observation that the data seemly obey a linear relationship. Moreover, on account of high noise level, we prefer a simpler model in general. The straight lines in Fig. 5.13 are the linear regression results and R^2 denotes the square of correlation coefficient which indicates the compactness. Compared with Fig. 5.13 (b) (compensated data via SCM), the data in Fig. 5.13 (c) (compensated data via ESCM) tend to be more compact which implies the shadowing errors are reduced in a more proper way via ESCM.

5.5 Conclusion Remarks

In this chapter, we have described an extension of the shadowing compensation model from restricted horizontal surfaces to more general inclined surfaces. The new model is derived by modeling image intensities in both the absence and presence of shadowing on general inclined surfaces. The new model does not include the restrictive assumption that shadowing effects exist only on horizontal surfaces. The experimental results show that the extended model, compared to the previous one, can achieve comparable performance on horizontal regions and even better performance on inclined surfaces.

Chapter 6. Conclusion and Future Works

In this thesis, we proposed a robust SEM photometric stereo using two BSE detectors, which can automatically produce a 3D shape and shadowless images under shadowing and noise conditions.

6.1 Summary

Validation of Gradient Equation

As SEM photometric stereo needs to compute gradient data from image pair before obtaining a 3D shape. The accuracy of gradient estimation is of essence for the final shape. As the Suganuma's gradient equation is experimentally found rather than theoretically deduced, we therefore design an experiment, in Chapter 2, to validate the effectiveness of the equation in our system setting. The basic idea is to check whether the gradients estimated by the equation are kept unchanged on the locus with an identical gradient. We realize that measurements are influenced by noise and the hypothesis can not hold exactly. We thus present an method to estimate the noise level from just a single image and estimate the standard deviation of the gradient measurements caused by image noise. The experiment has validated the effectiveness of Suganuma's equation.

SCM and ESCM

For eliminating shadowing errors, we model the physical process of shadowing generation. We have proposed two models in Chapter 3 and Chapter 5, respectively. One is SCM and the other is ESCM. Both are deduced in a analogous way by mathematically modeling image intensities in both cases of absence and presence of shadowing. These models relate the underlying shadowless image intensity to the observed one and provide a essential cue for de-shadowing. An advantage of SCM is that it takes a compact and implicit form. The simplicity makes it convenient for applications, when the assumption that the shadowing effects occur only on the horizontal surface holds approximately. As a typical instance, the assumed situation is generally common for measuring man-made structures such as semiconductors. Compared with SCM, ESCM is a more general model, where the shadowing can also occur on the inclined surfaces, i.e., the model accuracy is generally higher in a shadowed region with a considerably large sur-

face inclination. However, the numerical solution is required for ESCM, which makes it less computational efficient than SCM.

Variational Reconstruction and De-shadowing

Our proposed robust SEM photometric stereo is formulated as a constrained optimization problem via a variational approach. The objective functional consists of two terms. One is the fidelity term that is to guarantee the gradient of reconstructed shape should be consistent with the gradient data. In particular, the gradient data are evaluated from shadowless images so as to eliminate shadowing errors. In addition, shadowless images are related to the corresponding observed ones through our shadowing compensation model, which forms the constraints. The second term is total variation prior to penalize the roughness of the solution and consequently make our method be robust to noise influence arising in the data term. We adopt an iterative scheme to solve the problem, which performs commutatively between the compensation of image intensities and the modification of the corresponding 3D shape, can effectively provide both an accurate 3D shape and compensated shadowless images after convergence.

Advantages

There are several advantages of our proposed robust SEM photometric stereo. Firstly, the method can simultaneously handling shadowing and noise effects, which are most frequently occur or even inherent in imaging process. Secondly, the method is fully automatic with no need of human interactions. Finally, the method produces not only 3D shape, but shadowless images, which provides a potential opportunity for improving the imaging performance of SEM devices.

6.2 Discussions and Future Works

This thesis has established novel methods for robust SEM photometric stereo that can be used to solve problems with ill-conditions. In particular, the majority work is devoted to handling the shadowing problem, a considerably remaining challenge. The main contents discussed in this thesis are the establishment and utilization of SCM and ESCM. Listed below are further research possibilities that are identified during this study.

- A high speed implementation of our method has not yet been examined. We realize that it should be as a future work to improve the computational efficiency by means of exploring efficient numerical methods or parallel computing (GPU implementation, for instance).
- In the current study, we just simply choose the parameters in a manual manner.

However, we recognize this as a problem for future investigation requiring certain self-calibration techniques.

- Future studies designed to validate the feasibility of this approach in real applications are under consideration as well. For example, the proposed method should be evaluated on various semiconductor patterns in actual production lines with different processes and layouts. Moreover, we aim to utilize volume data from the estimated 3D surface as features for Automatic defect classification (ADC) [1, 22, 23], which may diversify the classification categories and improve the accuracy of the classification process. As yield prediction and specification of process issues in a production line are still very difficult, the proposed technology is expected to enhance quick and highly precise process control capabilities via synthetic analysis of a combination of information, in addition to ADC, including defect distribution, defect composition, equipment history, etc.

Acknowledgements

First of all, I would like to express my deep and sincere gratitude to Professor Shun'ichi Kaneko for supervising my dissertation and for introducing me to the fields of computer vision as well as SEM. I consider myself fortunate to have him as an advisor. At the very beginning of my doctoral course, I was just a freshman to the SEM fields and encountered a number of problems. He made a lot of considerations for me and gradually guided me into the structure of my research topic. His guidance is of essential importance for my study. Without his valuable advice and patient assistance, this study would not have been completed easily. In addition, he teach me generic ideas and methods for analyzing research problems. The abilities that I acquired from him will benefit me forever. He also teach me effective communication skills to other researcher, which will have a remarkable influence on my entire career.

I would like to thank Dr. Atsushi Miyamoto with the Yokohama Research Laboratory, Hitachi, Ltd., who act as my second supervisor. He is always willing to help and give his insightful comments and suggestions to my research. He also provide me selfless and patient help on paper writing and modification. For all this, I would like to express my deep thanks.

I would like to thank Associate Professor Takayuki Tanaka for his helpful suggestions and assistance in our laboratory. Professor Tanaka participates in many fruitful discussions concerning my research. I also want to thank the entire staffs and lab members in our laboratory for their friendship and help during the years of doctoral study.

I am grateful to my family for always supporting me in what I was doing.

Finally, the financial support from CSC is gratefully acknowledged.

References

[1] A. Miyamoto and T. Honda, "Development of Surface/Embedded Particle Classification Algorithm for SEM-ADC," IEICE Transaction on Information & Systems, Vol. J91-D, NO. 6, pp. 1604–1612, 2008.

[2] T. Oshima, S. Kimoto and T. Suganuma, "Stereomicrography with a Scanning Electron Microscope," Photogrammetric Engineering, Vol. 36, pp. 874–879, 1970.

[3] G. Koenig, W. Nickel, J. Storl, D. Meyer, and J. Stange, "Digital Stereophotogrammetry for Processing SEM Data," Scanning, Vol. 9, pp. 185–193, 1987.

[4] O. V. Kholodilov, A. Ya. Grigoryev and N. K. Myshkin, "Reconstruction of True Topographies of Solid Surfaces in Scanning Electron Microscopes Using Secondary Electrons," Scanning, Vol. 9, pp.156–161, 1987.

[5] J. Lebiedzik, "An Automatic Topographical Surface Reconstruction in the SEM," Scanning, Vol. 2, pp. 230–237, 1979.

[6] I. C. Carlsen, "Reconstruction of True Surface-Topographies in Scanning Electron Microscopes Using Backscattered Electrons," Scanning, Vol. 7, pp. 169–177, 1985.

[7] T. Suganuma, "Measurement of Surface Topography Using SEM with two Secondary Electron Detectors," Journal of Electron Microscopy, Vol. 34, NO. 4, pp. 328–337, 1985.

[8] L. Reimer, R. Böngerler and V. Desai, "Shape from Shading Using Multiple Detector Signals in Scanning electron Microscopy" Scanning Microscopy, Vol. 1, NO. 3, pp. 963–973, 1987.

[9] T. Czepkowski and W. Slówko, "Some Limitations of Surface Profile Reconstruction in Scanning Electron Microscopy" Scanning, Vol. 18, pp. 433–446, 1996.

[10] J. Paluszyński and W. Slówko, "Surface Reconstruction with the Photometric Method in SEM" Vacuum, Vol. 78, pp. 533–537, 2005.

[11] J. Paluszyński and W. Slówko, "Compensation of the Shadowing Error in Three-dimensional Imaging with a Multiple Detector Scanning Electron Microscope" Scanning, Vol. 224, pp. 93–96, 2006.

[12] L. Reimer, "Scanning Electron Microscopy: Physics of Image Formation and Microanalysis," 2nd ed. Springer, pp. 146–152, 2008.

[13] K. Sakaue, A. Amano and N. Yokoya, "Optimization Approaches in Computer Vision and Image Processing," IEICE Transactions on Information & Systems, Vol. E82-D, NO. 3, pp. 534–547, 1999.

[14] T. Poggio, V. Torre and C. Koch, "Computational Vision and Regularization Theory," Nature, Vol. 317, pp. 314–319, 1985.

[15] R. J. Woodham, "Photometric Method for Determining Surface Orientation from Multiple Images," Optical Engineering 19(1), pp. 139–144, 1980.

[16] D. Forsythe and J. Ponce, "Computer Vision: A Modern Approach," Prentice Hall, pp. 80–86, 2001.

[17] S. Barsky and M. Petrou, "The 4-Source Photometric Stereo Technique for Three-Dimensional Surfaces in the Presence of Highlights and Shadows," IEEE Transactions on Pattern Analysis and Machine Intelligence, Vol. 25, NO. 10, pp. 1239–1252, 2003.

[18] K. Ikeuchi and B. K. P. Horn, "Numerical shape from shading and occluding boundaries," Artificial Intelligence, Vol. 17, pp. 141–184, 1981.

[19] B. K. P. Horn and M. J. Brooks, "The Variational Approach to Shape from Shading," Computer Vision, Graphics and Image Processing, Vol. 33, pp. 174–208, 1986.

[20] B. K. P. Horn, "Height and Gradient from Shading," International Journal of Computer Vision, Vol. 5, pp. 37–75, 1990.

[21] I. N. Bronstein, K. A. Semendyayev, G. Musiol, H. Muehlig, "Handbook of Mathematics," Springer, fifth ed., 2007. ISBN 978-3540721215.

[22] K. Watanabe, Y. Takagi, K. Obara, H. Okuda, R. Nakagaki and T. Kurosaki, "Efficient Killer-defect Control using Reliable High-throughput SEM-ADC," Proc. The 12th Annual IEEE/SEMI Advanced Semiconductor Manufacturing Conference, pp.219–222, 2001.

[23] J. Ritchison, A. Ben-Porath and E. Malocsay, "SEM based ADC Evaluation and Integration in an Advanced Process Fab," Proc. SPIE, vol.3998, pp.258–268, 2000.

[24] C. R. Vogel and M. E. Oman, "Iterative Methods for Total Variation Denoising," SIAM Journal on Scientific Computing, Vol. 17, pp. 227–238, 1996.

[25] M. Fornasier, Ed., "Theoretical Foundations and Numerical Methods for Sparse Recovery," De Gruyter, 2010.

[26] T. Marschner and C. Stief, "Characterisation of 193nm Resist Layers by CD-SEM Sidewall Imaging," Proc. of SPIE, Vol. 5038, pp. 892–900, 2003.

[27] H. Morokuma, A. Miyamoto, M. Tanaka, M. Kazui and A. Takane, "New Technique to Reconstruct Effective 3D Profile from Tilt Images of CD-SEM," Proc. of SPIE, Vol. 5375, pp. 727–734, 2004.

[28] K. Setoguchi, H. Morokuma, A. Miyamoto and M. Tanaka, "Development of Beam-tilt Angle Calibration Technique for CD-SEM," Proc. of SPIE, Vol. 5752, pp. 1353–1361, 2005.

[29] T. Chan, J. Shen, "Image Processing and Analysis: Variational, PDE, Wavelet, and Stochastic Methods," SIAM 2005.

[30] A. Agrawal, R. Raskar and R. Chellappa, "What is the Range of Surface Reconstructions from a Gradient Field," ECCV, 2006.

[31] A. Bruhn, J. Weickert, T. Kohlberger and C. Schnorr, "A Multigrid Platform for Real-time Motion Computation with Discontinuity-preserving Variational Methods," International Journal of Computer Vision, Vol. 70, No. 3, pp. 257-277, 2006.

[32] N. C. Yew, "Dynamic Focusing Technique for Titled Samples in SEM," Proc. SEM Symp. IITRI, pp. 33, 1971.

[33] M. Schubert, A. Gleichmann, M. Hemmleb, J. Albertz and J. M. Kohler, "Determination of the Height of a Microstructure Sample by a SEM with a Conventional and a Digital Photogrammetric Method," Ultramicroscopy, Vol.63, No. 1, pp. 57 – 64, 1996.

[34] A. Carter, M. Ramsey, A. Durant and I. Skilling, "Micron-scale Roughness of Volcanic Surfaces from Thermal Infrared Spectroscopy and Scanning Electron Microscopy," Journal of Geophysical Research, 114, B02213 (2009).

[35] D. J. Stokes, F. Morrissey and B. H. Lich, "A New Approach to Studying Biological and Soft Materials Using Focused Ion Beam Scanning Electron Microscopy (FIB SEM)," Journal of Physics: Conference Series, Vol. 26, No. 1, pp. 50. IOP Publishing, 2006.

[36] C. Hernández and G. Vogiatzis and R. Cipolla, "Shadows in Three-Source Photometric Stereo," ECCV, 2008.

[37] Y. Yu and J. Chang, "Shadow Graphs and 3D Texture Reconstruction," IJCV, 62(1-2):35-60, 2005.

[38] Y. Yu and J. T. Chang, "Shadow Graphs and Surface Reconstruction," In ECCV, 2002.

[39] C. Manmohan, S. Agarwal and D. Kriegman. "Shadowcuts: Photometric Stereo with Shadows," Computer Vision and Pattern Recognition, 2007.

[40] William L. Briggs, Van Emden Henson, Steve F. McCormick, "A Multigrid Tutorial," Second Edition, SIAM, 2000.

[41] Ulrich Trottenberg, Cornelis Oosterlee and Anton Schuller, "Multigrid," Elsevier, 2001.

[42] P. Kornprobst and G. Aubert, "Mathematical Problems in Image processing, Partial Differential Equations and the Calculus of Variations," Springer 2006.

[43] F. Andreu, V. Caselles, J. I. Diaz and J. M. Mazon, "Qualitative Properties of the Total Vvariation Flow," Journal of Functional Analysis, 188(2):516–547, February 2002.

[44] G. Aubert, R. Deriche, and P. Kornprobst. "Computing Optical Flow via Variational Techniques," SIAM Journal on Applied Mathematics, 60(1):156–182, 1999.

[45] A. Bruhn, "Variational Optic Flow Computation: Accurate Modelling and Efficient Numerics," PhD thesis, Faculty of Mathematics and Computer Science, Saarland University, Germany, 2005.

[46] A. Chambolle, "An Algorithm for Total Variation Minimization and Applications," Journal of Mathematical Imaging and Vision, 20:89–97, 2004.

[47] T. Pock, A. Chambolle, D. Cremers and H. Bischof, "A Convex Relaxation Approach for Computing Minimal Partitions," IEEE Conference on Computer Vision and Pattern Recognition (CVPR), 2009.

[48] T. Chan and C. K. Wong, "Total Variation Blind Deconvolution," IEEE Transactions on Image Processing, 7(3):370-375, 1998.

[49] D. M. Young, "Iterative Solution of Large Linear Systems," Dover, New York, 2003.

[50] J. M. Morel and S. Solimini, "Variational Methods in Image Segmentation," Birkhauser, 1995.

[51] T. F. Chan and P. Mulet, "On the Convergence of the Lagged Diffusivity Fixed Point Method in Total Variation Image Restoration," SIAM Journal on Numerical Analysis, 36(2):354–367, 1999.

[52] C. Frohn-Schnauf, S. Henn and K. Witsch, "Nonlinear Multigrid Methods for Total Variation Denoising," Computating and Visualization in Sciene, 7(3-4):199–206, 2004.

[53] W. Hackbusch, "Multigrid Methods and Applications," Springer, New York, 1985.

[54] A. Ahmed and A. Farag, "Shape from Shading under Various Imaging Conditions," CVPR, 2007.

[55] R. Zhang, P. S. Tsai, J. Cryer, and M. Shah, "Shape from Shading: A Survey," IEEE Transactions on Pattern Analysis and Machine Intelligence, vol. 21, No. 8, pp. 690–706, 1999.

[56] J. Oliensis, "Uniqueness in Shape from Shading," International Journal of Computer Vision, Vol. 6, No. 2, pp. 75–104, 1991.

Appendix A Publication List

A.1 Journal Papers

1. D. Chen, A. Miyamoto and S. Kaneko, "Robust Surface Reconstructions in SEM using Two BSE Detectors," IEICE Transactions on Information and Systems, Vol.E96-D, No.10, pp. 2224–2234, Oct. 2013.

2. D. Chen, A. Miyamoto and S. Kaneko, "Extended Shadowing Compensation Model in Robust SEM Photometric Stereo," Journal of the Japan Society for Precision Engineering, Vol. 79, No. 10, pp. 1137–1144 , Nov. 2013.

A.2 International Conferences

1. D. Chen, A. Miyamoto and S. Kaneko, "Robust Surface Reconstruction in SEM with Two BSE Detectors," Proceeding of Mecatronics REM, pp. 64–70, 2012.

2. D. Chen, A. Miyamoto and S. Kaneko, "Extended Shadowing Compensation Model for Robust SEM Photometric Stereo," 11th International Conference on Quality Control by Artificial Vision, pp. 291–297, 2013.

3. D. Chen, A. Miyamoto and S. Kaneko, "Bootstrapping De-shadowing and Self-calibration in SEM Photometric Stereo," 20th Korea-Japan Joint Workshop on Frontiers of Computer Vision, pp. 68–75, 2014.

A.3 National Conferences (Japan)

1. D. Chen and S. Kaneko, "3D Surface Reconstruction in SEM via Relaxation Method," Proceedings of GCOE-NGIT 2011, October 5–6, 2011.

2. D. Chen and S. Kaneko, "3D Surface Reconstruction in SEM with Two BSE Detectors for Defector Analysis," The 5th International Symposium on Global COE Program of Center for Next-Generation Information Technology Based on Knowledge Discovery and Knowledge Federation (GCOE-NGIT 2012), January 16–18, 2012.

3. D. Chen, A. Miyamoto and S. Kaneko, "Extended Shadowing Compensation Model based De-shadowing in Robust SEM Photometric Stereo," Hokkaido University

Symposium on Alliance of Young Researchers in Information Science and Technologies 2013, March 7,8, 2013.

4. D. Chen, A. Miyamoto and S. Kaneko, "Robust Surface Reconstruction in SEM Using Two BSE Detectors," The Second International Joint Workshop on Intelligent Convergence Technology, July 22–24, 2013.